

Aspects of Hilbert space fragmentation in the quantum East model: fragmentation, subspace-restricted quantum scars, and effects of density-density interactions

Maitri Ganguli^{1*}, Sreemayee Aditya^{2*}, and Diptiman Sen²

¹*Department of Physics, Indian Institute of Science, Bengaluru 560012, India*

²*Center for High Energy Physics, Indian Institute of Science, Bengaluru 560012, India*

We investigate a one-dimensional correlated-hopping model of spinless fermions with an East constraint. We first analytically unravel the complete fragmentation structure of this model by labeling each fragment by a unique root configuration and utilizing the transfer matrix method. We show that the growth of the size of each fragment of the model follows the widely studied Dyck sequence, and is therefore analytically tractable with the help of Catalan triangles. While the eigenstate thermalization hypothesis (ETH) does not hold within the full Hilbert space which exhibits Poisson statistics of the energy level spacing, an examination of various quantities restricted to the largest fragments shows that a weaker version of the subspace-restricted thermalization holds. This weaker violation of the ETH within the largest fragments is supported by the presence of subspace-restricted quantum many-body scars due to quantum fragmentation. Our analysis further reveals that the filling fraction at which the model has the largest fragment shifts with increasing system sizes from half-filling due to the distinct fragmentation structure. Next, we show that the inclusion of a nearest-neighbor density-density interaction with strength V induces a spectral transition within the largest fragment from a weakly ETH-violating phase containing scars to a statistical bubble localized phase as V increases. In particular, the $V \rightarrow \infty$ limit produces an integrable model. We find that the addition of finite- V stabilizes the ground state near half-filling while keeping intact the fragmentation structure of the East model. However, this behavior abruptly changes exactly at $V = \infty$ due to the emergence of a distinct fragmentation structure; we analytically explore this in a comprehensive manner. The infinite- V model has many interesting properties, among which the appearance of the ground state and the largest fragment at two different filling fractions is specially noteworthy. Finally, we propose an experimental setup to realize the infinite- V model as a particular limit of a special kind of $t - V$ model with an on-site potential.

I. INTRODUCTION

Quantum many-body systems far from equilibrium have been extensively studied for many years across a variety of platforms, ranging from optical lattices through Rydberg chains with tunable interactions to superconducting processors¹⁻⁵. In this direction, the thermalization of an isolated many-body quantum system has been comprehensively explored over the past decade. The notion of thermalization in such systems has been formally comprehended with the help of the eigenstate thermalization hypothesis (ETH)⁶⁻⁹, which states that each eigenstate of a generic many-body strongly interacting quantum system implicitly carries the information of a thermal ensemble. As a consequence, these eigenstates self-thermalize on their own under time evolution.

The quest for finding novel forms of non-equilibrium universality has also shed light on various ergodicity-breaking mechanisms in many-body quantum systems¹⁰⁻¹³, which go beyond the ETH-satisfying family of models. The key quantity that plays a pivotal role in pinpointing the characteristics of such out-of-equilibrium many-body phases is quantum entanglement, which is also a central quantity from the viewpoint of quantum information processing¹⁴. These investigations thus lie at the frontier between quantum many-body physics and quantum information science, which is an active field of research in recent times due to the experimental advancements in diverse platforms¹⁻⁵.

It is known that models with kinetic constraints can give rise to several intriguing phenomena where the central mechanisms for the breakdown of quantum thermalization can range from quantum many-body scars^{11,15-18} to Hilbert space fragmentation^{11,19-27}. These quantum models also have received attention since considerable effort has been devoted in the past to investigating their classical counterparts, e.g., classical glasses undergoing a Markov evolution with kinetic constraints²⁸⁻³⁰.

The specific mechanism on which we will focus in this paper is Hilbert space fragmentation (HSF)¹¹, namely, a fracturing of the full Hilbert space into a number of fragments which grows exponentially with the system size; these different fragments may be integrable or non-integrable. Another fascinating feature of these fragmented systems is the presence of frozen eigenstates and blockades, which significantly impact the static and dynamical measures of thermalization in such systems. The frozen states are zero-energy eigenstates of the Hamiltonian, which do not participate in the dynamics. On the other hand, the presence of blockades forbids the dynamically active regions from interacting with one another. HSF can further be organized into two classes based on the growth of the largest fragment compared to the full Hilbert space size. Strong fragmentation^{11,26,31} refers to the case when the sizes of the largest fragments are exponentially smaller than the size of the full Hilbert space in the thermodynamic limit, whereas in weakly fragmented systems, the sizes of the largest fragments are smaller than the size of the full Hilbert space by only a power of the system size^{25,32,33}. There is an alternative classification possible in terms of the basis states, which defines the fragmentation structure of the full Hilbert space.

*These authors contributed equally to this work.

Classical fragmentation^{11,23,26} occurs when the fragmentation structure is defined in terms of the product of local basis states. When the fragmentation structure is defined in terms of entangled basis states, it is dubbed as quantum fragmentation^{23,25}. The different mechanisms can severely impact various measures of thermalization in a profound manner, yielding subspace- or Krylov-restricted thermalization^{11,19,20,26} to slow subdiffusive transport^{34,35} in such systems. In addition, there have been studies that investigate the prethermal HSF in driven systems which have no static counterparts^{36,37}.

In this paper, we will investigate a one-dimensional model of spinless fermions in which the Hamiltonian has terms involving three consecutive sites on a lattice. The model allows nearest-neighbor hoppings between sites j and $j + 1$ only when the left neighboring site $j - 1$ is occupied; such a constraint is called the East constraint^{25,33}. This model thus conserves the total particle number, but it breaks inversion symmetry. Furthermore, it is the most simple member of a recently introduced and a more general family of particle-conserving quantum East models²⁵. Our model is also known to exhibit a freezing transition^{32,33,38} as the filling is varied. The transition occurs at half-filling; there is strong fragmentation below half-filling and weak fragmentation above half-filling³³. Although the dimensions of the largest fragment at half-filling and above half-filling have been previously investigated while analyzing the freezing transition³³, the complete fragmentation structure and other effects of fragmentation have not been exhaustively explored for this model; this motivates our present study. We note that a complete analytical understanding of a fragmented Hilbert space is often challenging since the fragments cannot be labeled by the quantum numbers of local or quasilocal symmetry operators. The significant steps in this direction include constructs like statistically localized integral of motions³⁹, commutant algebras²³, and irreducible strings^{28–31,40,41}, and matrix-product operators²⁷, which successfully capture the fragmentation structures of several kinetically constrained models.

To unravel the complete fragmentation structure of the Hilbert space of this model, we first present a canonical representation of the root state by imposing some specific rules which uniquely label each fragment. This kind of procedure has been previously presented in the literature while studying the fragmentation structure of the Fredkin chain^{42–44}. The identification of root states enables us to count the total number of fragments and frozen states using the transfer matrix method^{29–31,45}. This further allows us to compute the growth of the Hilbert spaces with the system size for each of the fragments, followed by a mapping of the transitions allowed by the East constraint to the widely-studied combinatorics sequence of Dyck words. The growth of each fragment can thus be exactly analytically computed with the help of the total number of Dyck sequences appearing in the Catalan triangle of order $l = 1$ ⁴⁶. We have verified that our numerically obtained results are in complete agreement with our analytical findings.

A numerical study of short-range spectral correlations of the energy eigenvalues in this model indicates that although the ETH is not satisfied within the full Hilbert which shows

Poisson statistics, the largest fragments for all filling fractions follow the Krylov-restricted ETH^{11,20,26} in a weaker sense with the Gaussian orthogonal ensemble (GOE) statistics^{47–49}. The weaker violation of the ETH is confirmed by the presence of subspace-restricted many-body scars^{20,25}, which are the consequence of the recursive quantum HSF²⁵ within the classical fragments. Moreover, various static and dynamical measures of thermalization within the scar subspace reflect the signature of the ETH violation, which includes zero entanglement entropy of such eigenstates for certain entanglement cuts, the long-time revivals in the Loschmidt echo dynamics, and sudden jumps in the overlap amplitudes for the scar states which do not behave as smooth functions of the energy^{11,12}. We also observe that the filling at which the model has the largest fragment shifts from half-filling ($L/2$) as $\sqrt{L}/2$, where L is the system size; this can be readily confirmed using the asymptotic properties of the Catalan numbers⁴⁶. This shift also impacts the ground state properties since the ground state in this system lies within the largest fragment. Accordingly, we observe that the filling where the ground state appears also moves with increasing system sizes. In particular, the ground state never occurs at half-filling; this is a combined outcome of the fragmentation structure and the lack of inversion and particle-hole symmetry in this model.

To stabilize the ground state at a particular filling fraction, we investigate the effect of perturbations, namely, a nearest-neighbor density-density interaction with strength V , which is easily realizable in various experimental platforms^{1–4}. We note that a spectral transition occurs with increasing V from the GOE statistics (weakly ETH-violating case with subspace-restricted scars^{11,25,50,51}) to the Poisson statistics (statistical bubble localization within fragments^{52,53}). This statistical bubble localized phase^{52,53} is a manifestation of increasing V , which introduces large energy costs for certain configurations even within a fully connected fragment and eventually, for large V , produces secondary fragmentation within a single fragment due to the emergence of approximate conserved quantities. In particular, the $V \rightarrow \infty$ limit reduces to a constrained integrable model^{24,54}, which, interestingly, is invariant under inversion symmetry, unlike the East model with $V = 0$. We further note that increasing the value of V moves the ground state closer to half-filling while keeping the fragmentation structure of the East model intact. Nevertheless, this behavior abruptly changes exactly at the limit $V \rightarrow \infty$ due to the appearance of a different fragmentation structure. We analytically unravel the structure of this new fractured Hilbert space by mapping individual fragments to tight-binding models of non-interacting spinless fermions. This model displays some additional intriguing properties, such as the appearance of the largest fragment and of the ground state at two different filling fractions, which we are also able to explain analytically. Finally, we conclude by proposing an experimentally achievable special kind of $t - V$ model with a specific kind of on-site potential μ , which can give rise to this infinite- V model³¹ in a particular limit. The results obtained from our analysis in various limits have been schematically shown in Fig. 1.

The plan of this paper is as follows. In Sec. II, we intro-

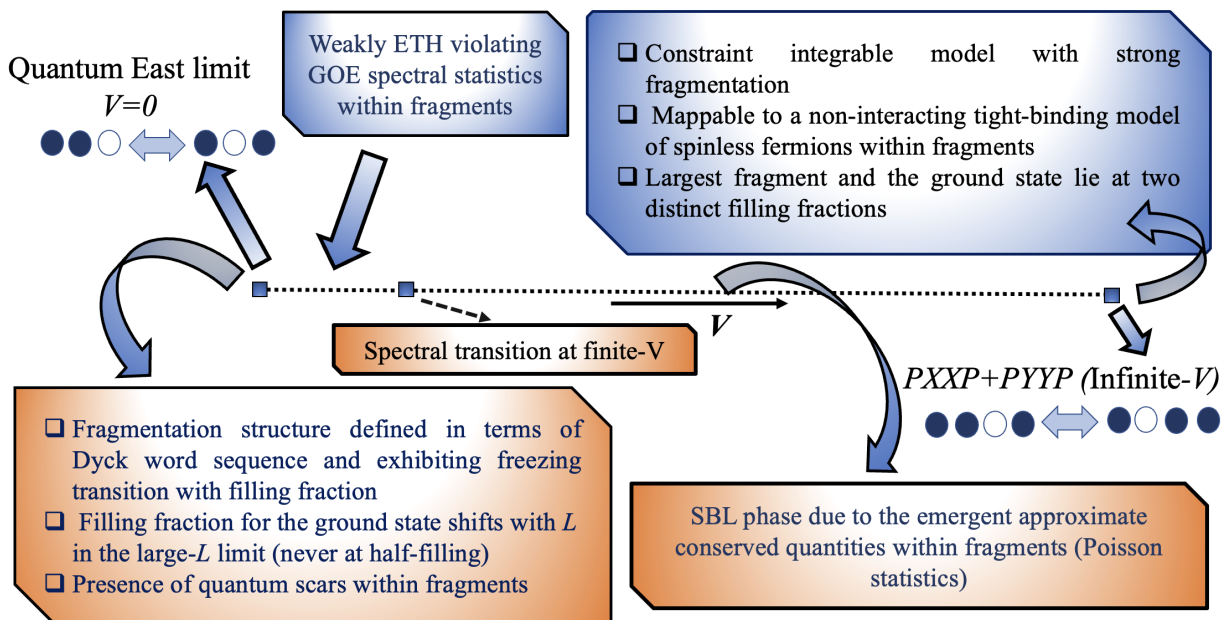


FIG. 1: Schematic of the main results obtained from our analysis. The PXXP+PYYP model will be discussed in Sec. IX, and the statistical bubble localized (SBL) phase will be discussed in Sec. VIII B.

duce our model and discuss the symmetries of the Hamiltonian. In Secs. III, we describe the fragmentation structure of this model after identifying the canonical representation for each root state identifying each fragment. Further, we discuss fragmentation-induced anomalous ground state properties of this model. Subsequently, we describe the ETH properties within the full Hilbert space and within fragments; additionally, we examine the recursive quantum HSF-induced subspace-restricted scar states in Sec. V. In Sec. VII, we investigate the dynamical signatures of the ETH violation within scar subspace; further, we also inspect the long-time behavior of autocorrelators, which exhibit distinct bulk and boundary characteristics. We afterward discuss the effects of interactions in the East model in Sec. VIII. In Sec. IX, we examine the infinite- V limit of this model, its fragmentation structure, and ground state properties. Further, we propose an experimental setup to realize this model in the same section. We then conclude this paper after summarizing our findings and offering the possible future avenues pertaining to this problem in Sec. X.

II. MODEL HAMILTONIAN

In this section, we introduce our correlated-hopping model which involves spinless fermions in one dimension with terms including three consecutive sites. The model allows nearest-neighbor hoppings between sites j and $j+1$ only if the site $j-1$ is occupied; this is called the strict East constraint. (This is known to be the simplest member of a more general family of facilitated correlated-hopping models with a similar kinetic

constraint²⁵). The Hamiltonian is given by

$$H = J \sum_j n_{j-1} (c_{j+1}^\dagger c_j + c_j^\dagger c_{j+1}), \quad (1)$$

where J denotes the strength of the hopping, and L is the system size. We will set $J = 1$ in the rest of this paper. While this model conserves the total particle number $N = \sum_j c_j^\dagger c_j$, and is invariant under translation symmetry (for a system with periodic boundary conditions (PBC)), it is not invariant under the inversion symmetry transformation given by $c_j \rightarrow c_{L+1-j}$. The energy eigenvalues of this Hamiltonian appear in pairs with $\pm E$ as a consequence of the sublattice symmetry transformation, given by $c_j \rightarrow (-1)^j c_j$, which transforms $H \rightarrow -H$.

III. FRAGMENTATION STRUCTURE OF THE EAST MODEL

Due to the dynamical hindrance caused by the East constraint, this model reveals an intriguing HSF structure, which we will now unravel using some analytical methods, namely, a transfer matrix method and enumerative combinatorics^{28–31,45} as discussed below.

A. Characterization of fragments using root configurations

We will first investigate how one can represent each fragment by a root configuration, which can label individual fragments in a unique manner. This identification will also pro-

vide an efficient way to characterize the fragmentation structure of the Hilbert space within this model^{11,31}, such as the total number of fragments and frozen states and the growth with the system size of all the fragments at arbitrary fillings; these properties have not been comprehensively explored before. We will assume open boundary conditions (OBC) for most of our analysis since this is more convenient for using the different analytical methods.

We first need to specify certain rules, which will enable us to characterize each fragment by a distinctive representative state; we will call this the root state for the rest of our discussion. To proceed, we note that the East constraint in our model only allows the transition

$$110 \leftrightarrow 101. \quad (2)$$

This can be represented in an equivalent form by using the notion of Dyck words^{42-44,46} in terms of open and closed parenthesis as $(() \leftrightarrow ())$, where 1 and 0 are replaced by an opening parenthesis, (, and a closing parenthesis,), respectively. Further we note that the number of opening and closing parenthesis along with the balanced pair of parenthesis, i.e., $()$ on both sides of the transition is the same. This suggests that the growth of each fragment can be captured via the extensively studied combinatorics sequence of Dyck words/paths⁴⁶. Next, it can be checked that for all simple and fully connected fragments, it is possible to move all occurrences of 10's to the leftmost end of the string by successively replacing 110's by 101's. This provides a canonical way of labeling each fragment by a distinct root state⁴²⁻⁴⁴. (We will discuss at the end of this section why the opposite procedure of replacing 101's by 110's does not guarantee a unique representation for root states). This method is identical to finding the faithful representations for all the equivalent classes as studied in representation theory. After successively removing all the 110's, the most general fully connected fragment can be represented by a unique root state with the following separable form $\psi_L \otimes \psi_m \otimes \psi_R$, where ψ_L can be a null string (ϕ) or a substring of 0's represented by $) \cdots ($ in the parenthesis notation, ψ_m is given by substrings of 10's or in an alternative notation by $() \cdots ()$, and ψ_R can be either a null string (ϕ) or a substring of 1's, i.e., $(\cdots ($ (or a substring of 0's followed by substring of 1's, i.e., $) \cdots ($). Thereafter, the dimension of such a fragment can be computed with the help of the following rules.

(i) One can always remove ψ_L from the counting problem since the transition does not allow it to participate in the dynamics. This statement also holds trivially when ψ_L is ϕ .

(ii) Subsequently, if ψ_R is a substring made of only 0's, i.e., $) \cdots ($ or any number of 0's followed by any number of 1's, $) \cdots ($, such a ψ_R also remains frozen under dynamical evolution. This statement again trivially holds when ψ_R is ϕ . These two scenarios comprise case I. But if ψ_R is a substring of 1's, i.e., $(\cdots ($, it has to be integrated into the counting problem; this gives rise to the second root category which we will call case II.

After implementing these rules, the growth of the dimen-

sion $D(L)$ of a fully connected fragment can be found from the Catalan triangle of order, $l = 1$ ⁴⁶, as follows.

(i) For the first case when ψ_R falls under case I, we obtain $D(L) = C(n, n)$, where $C(n, n)$ is the n -th Catalan number (diagonal elements of the Catalan triangle), given by $\frac{1}{n+1} \binom{2n}{n}$, and n denotes the number of 10's.

(ii) For the second case where ψ_R is a member of case II, we have $D(L) = C(n+k, n)$, where $C(n+k, n)$ is the element of the Catalan triangle of order $l = 1$ ⁴⁶ corresponding to $(n+k)$ -th row and n -th column, where n and k denote the total number of 10's and 1's in ψ_m and ψ_R , respectively. The element $C(p, q)$ associated to the p -th row and q -th column of the Catalan triangle of order $l = 1$ is given by $\binom{p+q}{q} - \binom{p+q}{q-1}$.

This procedure can be generalized further to an arbitrary string which contains blockaded regions that disconnect two active regions by frozen state configurations. All such strings containing blockades can thus be uniquely labeled by a root state with the following separable form $\psi_L \otimes \psi_{m_1} \otimes \psi_{I_1} \otimes \psi_{m_2} \otimes \psi_{I_2} \cdots \otimes \psi_R$, where ψ_L is a null string (ϕ) or a substring made of any number of 0's, ψ_{m_i} is a substring made of 10's, ψ_{I_i} is a blockade region comprising substring of 0's, and, finally, ψ_R contains only 0's or any number of 0's followed by any number of 1's or all 1's. The dimensions of such fragments with blockades can be computed with the help of similar rules as discussed above:

(i) For the first case with ψ_R falling under case I as discussed before, $D(L) = \prod_{i=1}^{L-1} C(n_i, n_i)$ where n_i is the number of pairs of 10's in ψ_{m_i} , and $C(n_i, n_i)$ is the n_i -th Catalan number.

(ii) For ψ_R with the properties of case II, $D(L) = \prod_{i=1}^{L-1} C(n_i, n_i) C(n_L + k, n_L)$, where n_i is the number of pairs of 10's in ψ_{m_i} and k is the number of 1's in ψ_R . Further, $C(n_L + k, n_L)$ denotes the element of the Catalan triangle corresponding to the $(n_L + k)$ -th row and n_L column, and $C(n_i, n_i)$ is the n_i -th Catalan number.

An equivalent representation of the Dyck words is possible in terms of Dyck paths. A Dyck path is a path that starts at the origin $(0,0)$ and ends at $(N, 0)$ in the two-dimensional $x-y$ plane; further, the path contains only two moves, namely, diagonal up steps $(1, 1)$ and diagonal down steps $(1, -1)$. Moreover, all Dyck paths have to meet the condition that they should always have $y \geq 0$. Following such a prescription, one can show the number of allowed Dyck paths with N moves is given by the Catalan number $D_{N,0,0} = \frac{1}{N/2+1} \binom{N}{N/2}$, where N is even. Furthermore, if we consider a more general case, where the paths start at $(0, 0)$ and end at (N, m) with $m \geq 0$, the number of allowed Dyck paths in the upper half

plane is given by

$$D_{N,0,m} = \frac{m+1}{N+1} \binom{N+1}{(N-m)/2}. \quad (3)$$

This is equal to the element of the Catalan triangle of order $l = 1$ corresponding to the n -th row and k -th column, where $n = (N+m)/2$ and $k = (N-m)/2$. We use the Dyck path representation to illustrate all the fragments, allowed states, and the dimensions of the fragments for the East model with $L = 5$ in Table I using the rules mentioned above.

Before ending this section, we note that we cannot find an alternate canonical representation for root states by successively replacing strings of 101's by 110's in this model. To show this, we consider the configuration 11001 as an example. It can be checked that this string is a member of a classical fragment specified by the root state 10101 due to our rule of successively replacing 110's by 101's. But if one replaces 101's by 110's instead, it may appear that the configuration 11001 is already a canonical root state as it does not contain any 101's to be replaced with 110's. However, this is clearly not true due to the fact if we start from the root state 10101 obtained using our earlier rule, and thereafter successively remove 101's, with the rule that the rightmost 101's are replaced first while replacing them with 110's, it will generate a different root state which is 11100 (by the transitions $10101 \rightarrow 10110 \rightarrow 11010 \rightarrow 11100$). This shows that replacing 101's by 110's fails to generate a unique root state for this fragment. Similar problems arise for several other fragments as well.

B. Counting of fragments

To characterize the fragmentation structure of our model, we will now count the total number of fragments as a function of L using the transfer matrix method. To do this, we will consider OBC which allows us to efficiently implement the above method. Using the fact that a unique identification of the root states requires us to remove all occurrences of 110's, we find that the number of fragments, N_{frag} , grows asymptotically as τ^L , where $\tau = (\sqrt{5}+1)/2$ is the golden ratio,^{28-31,45} as shown in Appendix A. Further, our analytical results are found to be in agreement with the values obtained by numerical enumeration.

The number of fragments N_{frag} for a given L can be analytically computed utilizing the fact that $N_{frag} = \sum_{i,j} M_{i,j}$, where $M = T_1^{L-2}$ for $L \geq 3$, and T_1 is the transfer matrix shown in Appendix A. This allows us to determine N_{frag} for the first few values of L , as shown in Table II. In addition, we choose $N_{frag}(L) = 1, 2, 4$ for $L = 0, 1, 2$, respectively, for further convenience.

We further note from Table II that N_{frag} follows the relation

$$N_{frag}(L) = F_{L+3} - 1, \quad (4)$$

where F_L is the Fibonacci sequence with initial conditions

$$F_0 = 0 \text{ and } F_1 = 1.$$

C. Frozen fragments

We will now discuss the growth of the total number of frozen fragments, which consist of a single state that does not participate in the dynamics. These states are eigenstates of our Hamiltonian with zero energy. The simplest examples of such states are $11 \cdots 11$ and $00 \cdots 00$. We can find the growth with the system size of these states using the transfer matrix method^{31,45} in the same way as the computation of the total number of fragments. Since the frozen states do not participate in dynamics, the transfer matrix for this computation should not have any 110 and 101's. Using this fact, a straightforward analytical calculation using the transfer matrix method^{28-31,45} demonstrates that $N_{froz}(L)$ grows as 1.466^L ; this again agrees with our numerically obtained results. The details of this computation, both with OBC and PBC, are shown in Appendix B.

D. Description of the largest fragment

After discussing the total number of fragments and frozen states, we will now find the filling fraction at which our model has the largest fragment. This question is important to address since it is already known that this model exhibits a freezing transition³³ as a function of filling. We will use our canonical representation method to answer this question. Before proceeding further, we note that the root identification method mentioned earlier already shows that the states in a fully connected fragment follow a specific sequence of the Dyck words⁴⁶, as shown in Sec. III A. Hence the growth of any fragment can be readily computed with the help of the Catalan triangle of order $l = 1$ after incorporating the rules discussed earlier. It can also be shown that the fully connected fragment with the largest dimension at a filling $N_f = L/2 + a$ with $a > 0$ is represented by the following root state $10 \cdots \cdots 1011 \cdots 1$. Following the rules discussed in Sec. III A, the dimension of such a fragment is found to be

$$D(L) = C(n+k, n) = \frac{(2a+1)}{(\frac{L}{2} + a + 1)} \frac{L!}{(\frac{L}{2} - a)! (\frac{L}{2} + a)!}, \quad (5)$$

where $n = (L/2 - a)$ and $k = 2a$ are the total number of 10's and 1's in ψ_m and ψ_R in the given root state, respectively. Since we are interested in the thermodynamic limit, we utilize




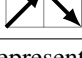
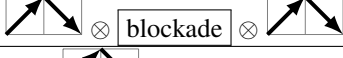



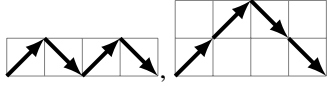
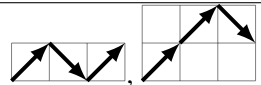
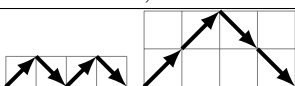
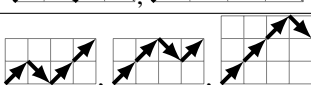
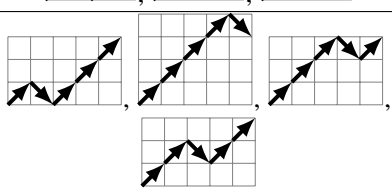
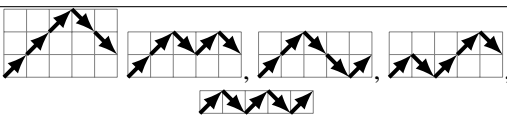
Root state	Allowed transitions within fragments	Dyck path representation (after implementing our rules)	D_{frag}
00000	00000	No representation (frozen state)	1
10000	10000	 (frozen state)	$C(1,0) = 1$
01000	01000	 (frozen state)	$C(1,0) = 1$
00100	00100	 (frozen state)	$C(1,0) = 1$
00010	00010	 (frozen state)	$C(1,0) = 1$
00001	00001	No representation (frozen state)	$C(1,0) = 1$
11111	11111	No representation (frozen state)	$C(5,0) = 1$
10010	10010	 $C(1,1) \times C(1,1) = 1$	$C(1,1) \times C(1,1) = 1$
10001	10001	 (frozen state)	$C(1,0) = 1$
00011	00011	No representation (frozen state)	$C(2,0) = 1$
01001	01001	 (frozen state)	$C(1,0) = 1$
10011	10011	 (frozen state)	$C(1,0) = 1$
00111	00111	No representation (frozen state)	$C(3,0) = 1$
01111	01111	No representation (frozen state)	$C(4,0) = 1$
10100	10100, 11000		$C(2,2) = 2$
00101	00101, 00110		$C(2,1) = 2$
01010	01010, 01100		$C(2,2) = 2$
01011	01011, 01101, 01110		$C(3,1) = 3$
10111	10111, 11110, 11101, 11011		$C(4,1) = 4$
10101	11100, 11010, 11001, 10110, 10101		$C(3,2) = 5$

TABLE I: Complete characterization of the fragmentation structure for $L = 5$ in the East model, showing the root state labeling each fragment, the allowed transitions within them, their Dyck path representations, and the dimensions of the fragments calculated using our rules.

L	3	4	5	6	7	8	9	10	11	12	13	14	15
N_{frag}	7	12	20	33	54	88	143	232	376	609	986	1596	2583

TABLE II: N_{frag} for the first few values of L as obtained analytically. These agree with our numerical results.

Stirling's formula, which gives

$$D(L) = 2^L \frac{(2a+1)}{\left(\frac{L}{2} + a + 1\right)} P,$$

$$\text{where } P = \sqrt{\frac{2}{2\pi L}} \left(1 - \frac{4a^2}{L^2}\right)^{-\frac{L+1}{2}} \left(1 + \frac{4a}{L}\right)^{-a}.$$
(6)

The above expression for P can be further simplified by taking a logarithm on both sides, expanding the expression up to $O(1/L)$, and then exponentiating the truncated series expansion; this thus yields $P \simeq \sqrt{\frac{2}{\pi L}} e^{-2a^2/L}$. Thereafter, the dimension of the largest fragment at a filling $N_f = L/2 + a$ reduces to

$$D(L) \simeq 2^{L+1} \frac{(2a+1)}{L} \sqrt{\frac{2}{\pi L}} e^{-\frac{2a^2}{L}}. \quad (7)$$

Extremizing the expression in Eq. (7), we obtain the filling fraction at which this model has the largest fragment,

$$\begin{aligned} N_f &= L/2 + a, \\ \text{where } a &= \frac{-\frac{1}{2} + \sqrt{\frac{1}{4} + L}}{2} \simeq \sqrt{L}/2. \end{aligned} \quad (8)$$

Eq. (8) implies that in the thermodynamic limit, the filling at which the largest fragment lies shifts away from half-filling ($L/2$) as $\sqrt{L}/2$ as L increases. We further numerically validate this result using Eq. (5), as shown in Fig. 2. In Fig. 2 (a-b), we plot $D(L)$ versus a for two large system sizes given by $L = 100$ and $L = 150$, respectively. Both the plots confirm that the largest fragment shifts as $L/2 + a$, where $a = \sqrt{L}/2$ is equal to 5 and 6 (approximately) for $L = 100$ and 150, respectively. We will later discuss how this shift impacts the ground state properties of this model in the thermodynamic limit.

We will now demonstrate that this model exhibits a freezing transition, i.e., a transition from strong fragmentation (below half-filling) to weak fragmentation (above half-filling) as a function of the filling fraction. The transition occurs exactly at half-filling. This has been shown in the literature³³ earlier while obtaining the growth of the largest fragment at half-filling using the Catalan numbers (the diagonal elements of the Catalan triangle) in a recursive manner³³. In this paper, we will validate this result utilizing our root identification method, which can capture this transition in a much easier manner. To do so, we need to first identify the appropriate root state representing the largest fragment at an arbitrary filling, and then find the growth of that fragment with the help of the Catalan triangle. To elucidate this below half-filling, let us consider the root state representing the largest fragment at a filling $N_f = L/2 - \alpha L$, where we assume that $0 < \alpha \ll 1$. We note that such a root state has the following form $0 \cdots 010 \cdots 10$ or $10 \cdots 100 \cdots 0$, where the numbers of 10's in the ψ_m part of the root state is $(L/2 - \alpha L)$, and $2\alpha L$ is the number of 0's in ψ_L or ψ_R , respectively. Now, given such a root state, the dimension, $D(L)$ of such a fragment can be readily obtained using the rules given in Sec. III A, as

$$\begin{aligned} D(L) &= C \left(\frac{L}{2} - \alpha L, \frac{L}{2} - \alpha L \right) \\ &= \frac{1}{L/2 - \alpha L + 1} \frac{(L - 2\alpha L)!}{((L/2 - \alpha L)!)^2}. \end{aligned} \quad (9)$$

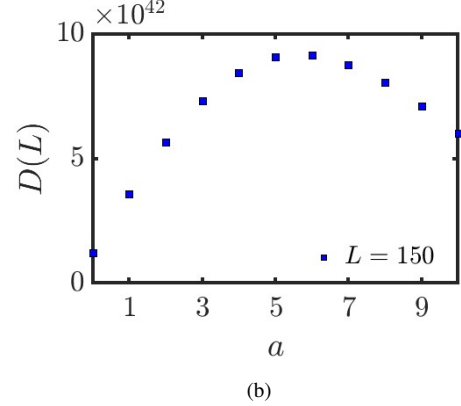
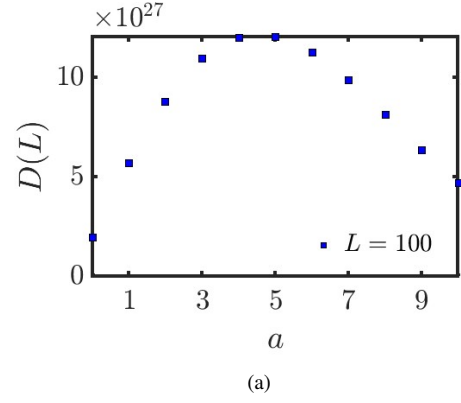


FIG. 2: (a-b) Plots showing the dimension of the largest fragment given by $D(L)$ (obtained using the Eq. (5) versus a , where the filling, $N_f = L/2 + a$ for $L = 100$ and $L = 150$, respectively. These two plots confirm that $D(L)$ appears to be largest for $L/2 + a$ where $a \simeq \sqrt{L}/2$ in the large- L limit, which is 5 and 6 for $L = 100$ and 150, respectively.

Using Stirling's formula, the above expression can be recast as follows in the large- L limit,

$$\begin{aligned} D_{max}(L) &\simeq \frac{\mu^L}{L^{3/2}}, \\ \text{with } \mu &\simeq 2^{1-2\alpha}, \end{aligned} \quad (10)$$

to lowest order in α .

On the other hand, the dimension of the full Hilbert space for $N_f = L/2 - \alpha L$, D_{sum} is given by

$$D_{sum}(L) \simeq \frac{L!}{(L/2 - \alpha L)!(L/2 + \alpha L)!}, \quad (11)$$

which in the large- L limit becomes $2^L e^{-2\alpha^2 L} / \sqrt{L}$ to lowest order in α , utilizing Stirling's formula. Eqs. (10) and (11) thus indicate that $D_{max}(L)/D_{sum}(L) \rightarrow 0$ exponentially as $L \rightarrow \infty$ for $\alpha > 0$. This implies strong fragmentation below half-filling. However, as one approaches half-filling, we find that $D_{max}(L)/D_{sum}(L) \simeq 1/L$, which means this ratio again goes to zero in the thermodynamic limit, but only polynomially, which is much slower than an exponential fall.

This, therefore, signifies a change in the fragmentation structure, and therefore, $N_f = L/2$ is called the critical filling fraction for the strong-to-weak fragmentation transition. One can perform a similar analysis for the Hilbert space above half-filling, where the ratio $D_{max}(L)/D_{sum}$ for $N_f = L/2 + a$ with $a > 0$ reduces to

$$\frac{D_{max}(L)}{D_{sum}(L)} = \frac{2a + 1}{L/2 + a + 1}, \quad (12)$$

where $D_{max}(L)$ is given in Eq. (5) and D_{sum} is the dimension of the full Hilbert space for $N_f = L/2 + a$. If we write $a = cL$ (where c is a number of order 1) and $L \rightarrow \infty$, Eq. (12) reduces to $\simeq 4c/(2c + 1)$, which is a constant in the thermodynamic limit. This thus validates the fact that this model manifests a weakly fractured Hilbert space above half-filling.

IV. GROUND STATE PROPERTIES OF THE EAST MODEL

We will now discuss some of the anomalous ground state properties of the East model; these are consequences of the unusual fragmentation structure of the Hilbert space. It is well-known that understanding the ground state is crucial for comprehending the low-energy properties of many-body quantum systems. However, it has recently been observed that a fractured Hilbert space can give rise to anomalous ground state behavior^{31,42,43,55}, which can significantly impact the low-energy properties of such systems, as we will show in the discussion below. We have already established earlier that the filling at which this model has the largest fragment shifts from half-filling as $L/2 + \sqrt{L}/2$. In addition, a numerical exact diagonalization analysis of the full Hilbert space and of specific fragments confirms that the ground state lies within the largest fragment, regardless of the boundary conditions (OBC or PBC). Qualitatively, this occurs since the larger dimension of a fragment usually favors the reduction of the minimum energy eigenvalue cost (although there are some exceptions). Accordingly, the filling fraction for the ground state also shifts from half-filling as $\sqrt{L}/2$ in the large- L limit; this is a consequence of the distinct fragmentation structure of this model. In Figs. 3 (a-b), we demonstrate the shift of the ground state filling as a function of L with PBC and OBC, respectively, for small system sizes. In both cases, we observe that the ground state energy E_{GS} lies at $N_f = L/2 + 2$ for $L = 10, 12, 14$, and $N_f = L/2 + 3$ for $L = 16, 18$ and 20 , respectively. One should note that the shift in filling for the ground state as $\sqrt{L}/2$ is an asymptotic result; however, this finite-size behaviors shown in Fig. 3 does indicate that there is a shift in the filling for the ground state as one increases the system size.

V. ETH PROPERTIES OF THE HILBERT SPACE

In this section, we will discuss the thermalization properties of the Hilbert space of this model. In fragmented systems, the presence of exponential numbers of frozen eigenstates, integrable fragments, and blockades typically causes a

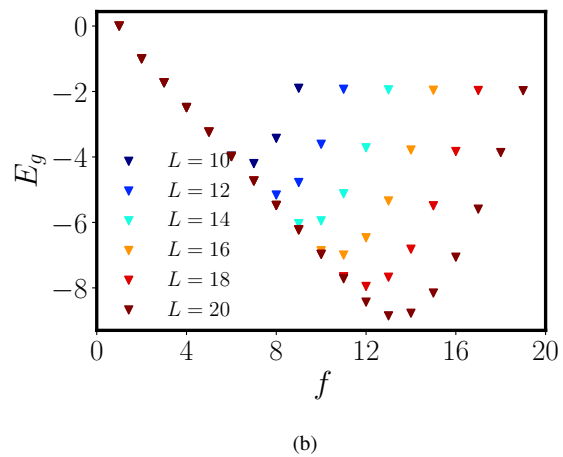
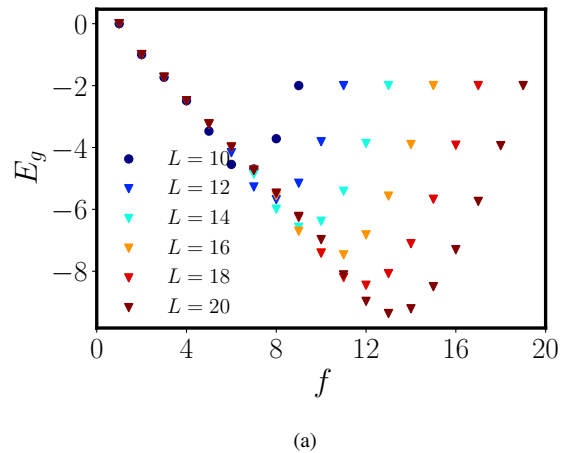


FIG. 3: (a-b) Plots showing the ground state energy E_g as a function of filling f for the East model with PBC and OBC, respectively, for different system sizes. Both plots confirm a shift in the filling away from $L/2$ for the ground state.

complete breakdown of the ETH within the full Hilbert space. At the same time, fragmentation can also yield novel thermalization properties within the different subspaces, which is called Krylov- or subspace-restricted thermalization^{11,20,31}. Furthermore, there are also some models known where quantum many-body scars are found within some of the fragments. We will now elucidate the complete thermalization properties of our model within the full Hilbert space and within individual fragments in the following sections.

A. ETH properties within the full Hilbert space at different fillings

We will first inspect the bipartite entanglement spectrum for the full Hilbert space for different fillings, i.e., at half-filling, above half-filling, and below half-filling. As this model manifests weak and strong fragmentation above and below half-

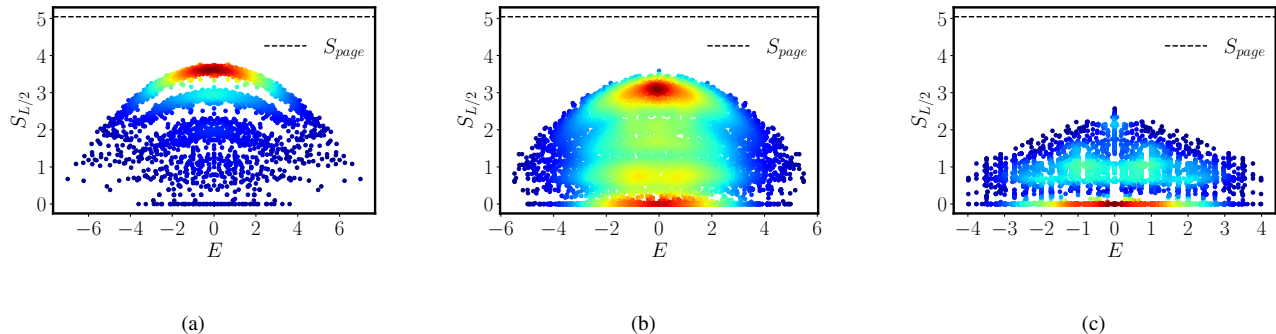


FIG. 4: Plots showing the half-chain entanglement entropy $S_{L/2}$ versus E for the full Hilbert space for $L = 16$ for three different fillings, i.e., $L/2 + 3$ (above half-filling), $L/2$ (at half-filling) and $L/2 - 2$ (below half-filling). In all cases, the maximum value of $S_{L/2}$ is much below the Page value, S_{page} , as depicted by the red dashed line. (a) For $N_f = L/2 + 3$, the entanglement spectrum shows several well-defined rainbow patterns, with the majority of states lying within the uppermost rainbow pattern. (b) For $N_f = L/2$, the entanglement spectrum shows that several rainbow patterns are beginning to separate from one another, and the major fraction of states lie in either the uppermost rainbow or in the states with zero entanglement. (c) For $N_f = L/2 - 2$, the entanglement spectrum looks quite different from the other two cases. The rainbow patterns have coalesced to form an almost continuous entanglement spectrum, and there is a large number of states with zero entanglement.

filling³³, respectively, one might expect that the entanglement spectrum for the different cases should be distinct from one another. In Figs. 4 (a-c), we show the half-chain entanglement $S_{L/2}$ versus the energy E for $L = 16$ for three different fillings given by $N_f = L/2 + 3$, $L/2$ and $L/2 - 2$. In all cases, we see that the value of $S_{L/2}$ is much lower than the Page value given by $S_{\text{page}} = \frac{1}{2}(L \ln(2) - 1)$ ⁵⁶; this implies that the ETH is not satisfied within the full Hilbert space. In addition, the entanglement spectrum also carries the signature of the freezing transition^{32,33}; this can be argued as follows. In Fig. 4 (a), we see that there are several well-defined rainbow patterns separated from one another; moreover, the majority of states lie in the uppermost rainbow pattern, which signifies that the largest fragment at this filling grows faster than all the other fragments. However, Fig 4 (c) reveals that there are no separated well-defined rainbow patterns for $N_f = L/2 - 2$; rather, there is a smooth spectrum of the entanglement entropy where the largest value of $S_{L/2}$ is much lower than the S_{page} due to the strong fragmentation below half-filling. Also, the maximum density of states lies near the states with $S_{L/2} \simeq 0$, which is primarily governed by the frozen eigenstates and by fragments consisting of active regions separated by blockaded regions. In addition, exactly at the freezing transition point^{32,33}, i.e., at $N_f = L/2$, we note an intermediate behavior in the entanglement spectrum. To be specific, we see that several well-defined rainbow patterns are beginning to form, and at the same time, the majority of states divide themselves into two regions, in the uppermost rainbow pattern (dominant region for above half-filling) as well as in the region comprising the zero-entanglement eigenstates (dominant region for below half-filling). This intermediate characteristic occurring at half-filling also points towards a transition occurring at this filling fraction.

To understand the ETH properties within very large fragments, we consider the largest fragment of the full Hilbert

space for $L = 18$; this occurs at $N_f = L/2 + 3$ with the fragment dimension equal to 9996. As shown in Fig. 5, we note a well-defined rainbow pattern, characteristic of a thermalizing system, with a number of states with exactly zero entanglement lying near the middle of the spectrum. The zero-entanglement states can be potential candidates for quantum many-body scars. The rainbow pattern implies that sufficiently large fragments thermalize within their own Hilbert spaces, but in a weak sense. This weak violation of Krylov-restricted thermalization is supported by the presence of subspace-restricted quantum many-body scars^{20,25,50,51} as discussed below. In addition, we note that although all sufficiently large fragments follow the weak form of Krylov-restricted thermalization for all fillings, the number of outlying states that violate the ETH⁶⁻⁸ increases as one moves from weak to strong fragmentation side, i.e., from above to below half-filling.

Another standard measure for checking the integrability⁵⁷ or non-integrability⁴⁹ of a model is the nearest-neighbor energy eigenvalue correlation^{58,59}, namely, the level spacing statistics between consecutive energy eigenvalues in the sorted energy spectrum. However, the level spacing analysis of consecutive energy levels is often difficult in many-body quantum systems since it needs an appropriate unfolding procedure, which requires us to know the exact form of the density of states⁴⁷. However, the extraction of the density of states is prohibitively hard in many cases. To circumvent this problem, it is preferable to analyze the spectral statistics in terms of the ratio of two consecutive level spacings of the sorted energy spectrum^{47,60}. This is defined as $r_n = \delta_{n+1}/\delta_n$, where $\delta_n = E_{n+1} - E_n$ with E_n being the n -th energy eigenvalue. This ratio analysis does not require any information on the profile of the density of states in such systems, which makes it more convenient to study than the level spacing statistics. Now, it is well-established that integrable systems follow the

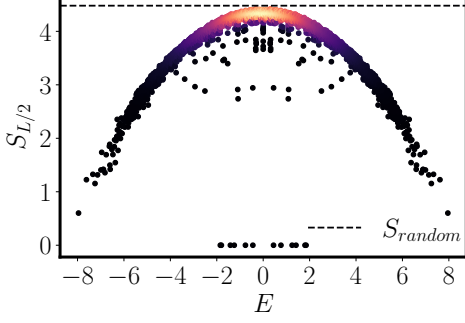


FIG. 5: Plot exhibiting $S_{L/2}$ versus E in the largest fragment for $L = 18$ and filling $N_f = L/2 + 3$; the fragment dimension is 9996. We observe a sharp, well-defined rainbow pattern, where the maximum value of $S_{L/2}$ is much smaller than S_{page} for the full Hilbert space; nevertheless, it almost reaches the value of $S_{L/2}$ for a typical thermal random state within the fragment.

the Poisson distribution^{47,57,60} due to the lack of any level repulsion in the energy spectrum with the form

$$P(r) = \frac{1}{(1+r)^2}, \quad (13)$$

while a non-integrable model in the presence of time-reversal symmetry obeys the GOE statistics^{47,49,59,60} given by the random matrix theory of real Hermitian Hamiltonians as

$$P(r) = \frac{27}{8} \frac{(r+r^2)}{(1+r+r^2)^{5/2}}. \quad (14)$$

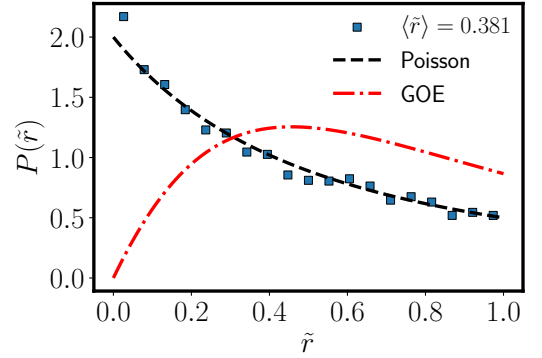
It is further convenient to introduce a variable \tilde{r} rather than r , which is given by

$$\tilde{r}_n = \frac{\min(\delta_{n+1}, \delta_n)}{\max(\delta_{n+1}, \delta_n)} = \min(r_n, 1/r_n). \quad (15)$$

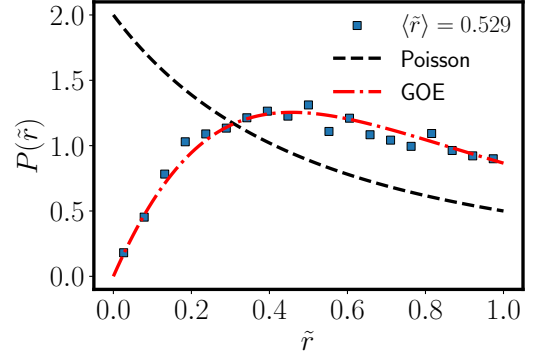
We note that \tilde{r} follows the distribution $P(\tilde{r}) = 2P(r)\theta(1-r)$, where $\langle \tilde{r} \rangle = 0.536$ and 0.386 for the GOE and the Poisson distributions, respectively.

In Figs. 6 (a-b), we have shown the distribution of consecutive level spacing ratios within the full Hilbert space for half-filling and within the largest fragment for filling $N_f = L/2 + 3$ for $L = 16$ and 18 , respectively, with OBC. In both cases, we introduce a small diagonal disorder of strength $w = 0.01$ in order to break any undesirable discrete symmetries as well as to circumvent any accidental degeneracies^{20,31,61}, which can potentially create ambiguities in the level spacing analysis. We note that the presence of a diagonal disorder keeps the fragmentation structure of the East model intact. In Fig. 6 (a), we observe that the level statistics of the full Hilbert space is indistinguishable from the Poisson statistics^{31,61,62} due to the presence of exponentially many invariant subspaces, which act as conserved quantities and thus prevent any level repulsion in the spectrum. On the other hand, Fig. 6 (b) depicts that

the largest fragment at $N_f = L/2 + 3$ demonstrates the GOE distribution^{20,31,61,62}, which implies that the model within the largest fragment is non-integrable, further reflecting the signature of a weaker version of the Krylov- or subspace-restricted ETH^{11,20,31} within this fragment. One should note that this weak violation of the ETH within sufficiently large fragments is supported by several exactly zero-entanglement eigenstates for specific entanglement cuts in the middle of the spectrum, as pointed out in Fig. 5. These zero-entanglement eigenstates within the sufficiently large fragments are candidates for quantum many-body scars^{20,25,50,51}, which will be the central object for the next part of our discussion.



(a)



(b)

FIG. 6: (a-b) The distribution of consecutive level spacing ratios for the full Hilbert space at $N_f = L/2$ and for the largest fragment for $N_f = L/2 + 3$, for system sizes $L = 16$ and $L = 18$, respectively. We include a small random on-site potential with $w = 0.01$ in order to break any accidental degeneracy and undesired discrete symmetries. (a) We observe that the level spacing ratios follow the Poisson distribution for the full Hilbert space. (b) The level spacing ratio within the largest fragment obeys the GOE distribution.

VI. RECURSIVE QUANTUM HILBERT SPACE FRAGMENTATION AND MANY-BODY SCARS

As mentioned earlier, there are many exact zero-entanglement states near the middle of the spectrum within almost all fully connected and sufficiently large fragments in the East model; this is also illustrated in Fig. 5. These zero-entanglement states demand a more thorough investigation since they show features similar to quantum many-body scars^{15,16,63,64}. Scars have been extensively studied in models with kinetic constraints, for instance, the PXP model^{12,15}. However, in our case, similar states emerge within HSF-induced fragments; hence we call them subspace-restricted scars. Such scars have been found before in other fragmented systems^{20,25,50,51}. Before proceeding further, we note that quantum many-body scars are highly-excited eigenstates of non-integrable quantum many-body systems which violate the ETH in a weak sense. This is a weak violation⁶⁻⁸ in the sense that almost all the eigenstates of such systems satisfy the ETH, except for the scar states^{15,16,63} which form a set of measure zero in the thermodynamic limit. This partial violation of the ETH can significantly affect the non-equilibrium dynamics of such many-body systems^{11,12}. For instance, quantities such as the Loschmidt echo and the occupation number starting from an initial product state which has a high overlap with such scar-like states show long-time persistent revivals under unitary time evolution. This is which is a prominent signature of the system retaining the memory of the initial state for a long period of time.

To begin our analysis of scars, we observe that there are twelve exact zero-entanglement states in the middle of the spectrum for a bipartite entanglement cut within the largest fragment for $L = 18$ and $N_f = L/2 + 3$ (this fragment has dimension 9996); this is shown in Fig. 5. This number is surprisingly small compared to the Hilbert space dimension of this fragment. Next, we plot the wave functions of these states to investigate the number of Fock basis states with which these states have significant overlaps. In Fig. 7 (a), we demonstrate the wave function of a scar eigenstate. We find, surprisingly, that it has a non-zero overlap with only 21 basis states in the Fock space, showing that it has the following separable form, $|\phi_L\rangle \otimes |00\rangle \otimes |\phi_R\rangle$, where $|\phi_L\rangle$ is either $|11100110\rangle$ (for the first 7 basis states), $|11010101\rangle$ (for the second 7 basis states) or $|10111001\rangle$ (the third 7 basis states). Furthermore, $|\phi_R\rangle$ are all the possible basis states for a subsystem with 8 sites and 7 particles having the constraint that the leftmost particle is strictly frozen in all the basis states. In fact, it can further be shown that the left-restricted part of these scar eigenstates is $|\phi'_L\rangle = \frac{1}{\sqrt{3}}(|11100110\rangle - |11010101\rangle + |10111001\rangle)$; this is an eigenstate with zero eigenvalue of the left-restricted Hamiltonian with $L = 8$ and $N_f = 5$. Further, we note that this left-restricted eigenstate is a zero-energy eigenstate of a classical fragment labeled by the root state 10101111. This left-restricted part cannot interact with the right part, $|\phi_R\rangle$ due to the intermediate blockaded region given by $|00\rangle$. Consequently, the dynamics of such a scar subspace essentially comes from the $|\phi_R\rangle$ part, which can be described by an effective Hamiltonian within the basis of seven

product states, i.e., $|11111110\rangle$, $|11111101\rangle$, $|11111011\rangle$, $|11110111\rangle$, $|11101111\rangle$, $|11011111\rangle$, and $|10111111\rangle$. The effective Hamiltonian within this right-restricted part reduces to a single hole hopping in a background of 7 particles (the leftmost particle is frozen) with OBC. The single-particle dispersion of this effective problem is given by $E_p = -2\cos(\pi p/8)$, where $p = 1, 2, \dots, 7$; this has the eigenvalues $E = \pm 1.8476, \pm 1.414, \pm 0.7654$, and 0. We have then numerically verified that 6 out of the total 12 scar states within this fragment appear to have the same analytically obtained eigenvalues, except for the state with $E = 0$. The zero-energy scar state does not disappear, but it becomes numerically difficult to isolate it due to the presence of a large number of zero-energy thermal (i.e., non-scar) states which can hybridize with the scar state. We note that it is absolutely crucial to consider appropriate entangled combinations of left-restricted basis states to understand the many-body scars described above. This bears a close analogy to quantum fragmentation²³; however, the crucial difference with the usual quantum fragmentation lies in the fact that our scars occur within the classical fragments in a recursive manner²⁵. This feature was first demonstrated in the longer-range variant of the East model discussed in Ref. 25.

In the fragment described above, we have identified another six scar states, whose left-restricted part is again a zero-energy eigenstate of the East model for a smaller subsystem with $L = 9$ and $N_f = 6$, and has the form $|\phi'_L\rangle = \frac{1}{2}(|101111100\rangle - |110111010\rangle - |111100101\rangle + |111010110\rangle)$. This is a member of the classical fragment which has the root state, 101010111. The left-restricted part is once again separated from the right-restricted part by a blockades part given by $|00\rangle$. Finally, the right-restricted part only participates in the dynamics as in the previous case, and the dispersion can be captured by a tight-binding model with $L = 7$ and OBC, where a hole hops in the background of 6 particles, with the leftmost particle being strictly frozen. The dispersion of the rightmost part is described by $E_p = -2\cos(\pi p/7)$, where $p = 1, 2, \dots, 6$. The energy eigenvalues are therefore $\pm 1.2469, \pm 0.445$, and ± 1.8019 .

In Fig. 7 (b), we show the density profile for a scar state as a function of the site index i . This illustrates that the scar state has a product part given by $|00\rangle$ exactly at $i = 9$ and 10 . This makes the entanglement S_l exactly equal to zero if the bipartite cut is made at $l = 9$ and 10 , as shown in Fig. 7 (c). Fig. 7 (b) also shows that the leftmost site of $|\phi_R\rangle$ is frozen at $n_i = 11$; this again gives zero entanglement if a cut is made at $l = 11$, as we see in Fig. 7 (c).

In Figs. 8 (a-b), we examine the expectation values of the few-body observables $n_{L/2}$ and $n_{L/2}n_{L/2+1}$ in all the eigenstates within the largest fragment for $L = 18$ and $N_f = L/2 + 3$ (this fragment has 9996 states). The expectation values of these observables appear to be a smooth function of the energy for almost all the eigenstates, except for a few outlying states near the middle of the spectrum which are the scar eigenstates within this fragment; these states lead to a weak violation of ETH. Furthermore, $\langle s_j | n_{L/2} | s_j \rangle$ and $\langle s_j | n_{L/2} n_{L/2+1} | s_j \rangle$ turn out to be zero for the scar eigenstates, where s_j denotes the j -th scar state. The zero ex-

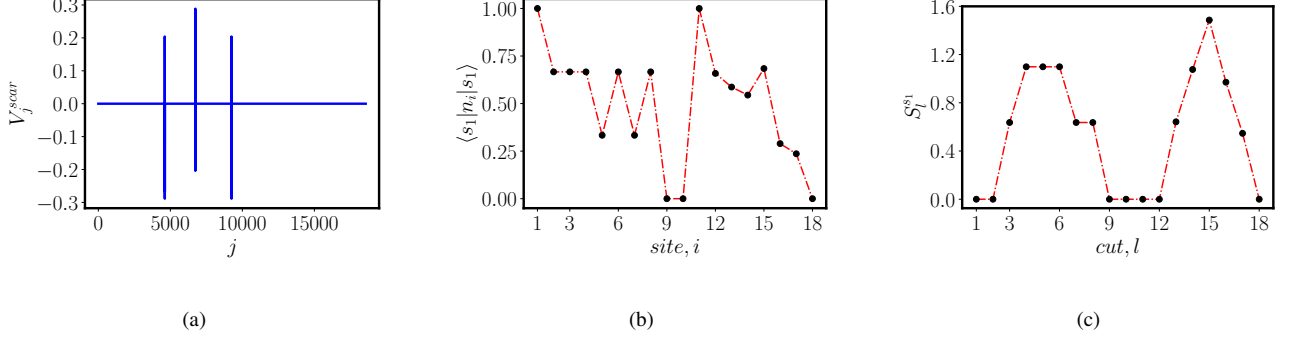


FIG. 7: (a) Plot showing the structure of the wave function for a scar eigenstate within the largest fragment of $L = 18$ and $N_f = L/2 + 3$ (the fragment contains 9996 states). This scar has a non-zero large overlap with exactly 21 Fock basis states, which is much smaller than the size of the full Hilbert space size. (b) The density profile of a scar eigenstate $|s_1\rangle$ versus the site index i for a specific scar state within this fragment, which appears to have a state $|00\rangle \otimes |1\rangle$ at sites $i = 9, 10$, and 11 . (c) The entanglement entropy S_l versus the position l of the cut for the same scar state shows zero entanglement at $l = 9, 10, 11$, and 12 ; this is the consequence of the specific product form of these scar states.

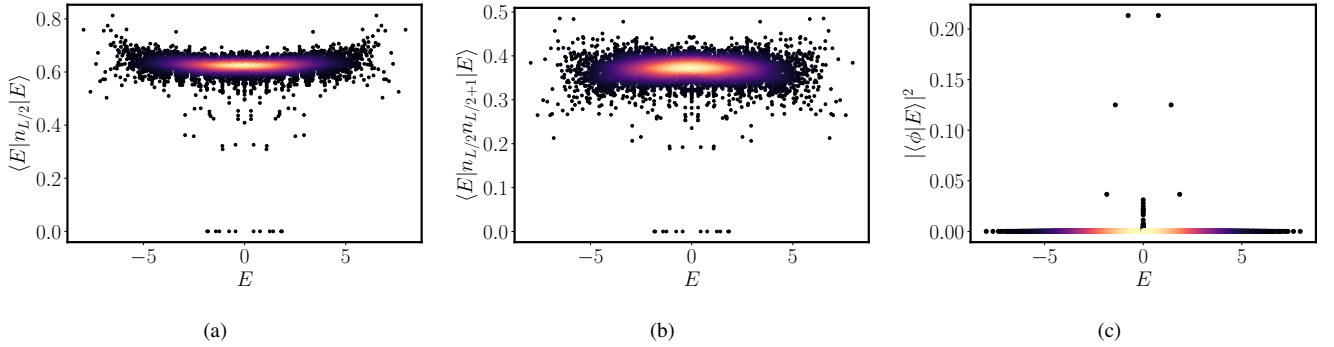


FIG. 8: (a-b) Plots showing the expectation values of $n_{L/2}$ and $n_{L/2}n_{L/2+1}$ in the eigenstates lying in the largest fragment for $L = 18$ and $N_f = L/2 + 3$. (c) The overlap of a specific state $|\phi\rangle$ (whose left-restricted part is a zero-energy eigenstate of the Hamiltonian for the East model with 8 sites and 5 particles) with all other eigenstates within this fragment. Plots (a-b) demonstrate that both expectation values are smooth functions of E except for a few eigenstates in the middle of the spectrum. (c) We see that the state $|\phi\rangle$ has large overlaps with only six eigenstates which have $E \neq 0$. In addition, this state has small overlaps of the order of 10^{-2} with a number of states at $E = 0$.

pectation values can be explained from the structures of these states, which has the form $|00\rangle$ on the sites $j = L/2 = 9$ and $j = L/2 + 1 = 10$; this leads to the zero expectation values for these states. In Fig. 8 (c), we consider the state

$$|\phi\rangle = \frac{1}{\sqrt{3}} (|11100110\rangle - |11010101\rangle + |10111001\rangle) \otimes |00\rangle \otimes |11111110\rangle \quad (16)$$

with which the scar states have a large non-zero overlap, and we show the overlap amplitudes of this state with all the eigenstates as a function of E within the fragment; the figure is consistent with what we see in Figs. 8 (a-b). We then note that there are exactly six eigenstates with $E = \pm 1.8478, \pm 1.414, \pm 0.7654$, which have a large overlap of order 1, as expected from our previous discussion. These sudden jumps in the overlap amplitudes suggest that this quantity is not a smooth function of E . This is not a behavior expected from the ETH^{6-8,11,12}, and these six eigenstates therefore vio-

late the ETH^{6-8,11,12} within the fragment. At the same time, we observe another bunch of few eigenstates with $E = 0$ showing a small overlap of the order of 10^{-2} with the given state. This is probably due to the zero-energy eigenstate of the scar subspace, which gets hybridized with other thermal zero-energy states during numerical diagonalization. Accordingly, these zero-energy states also demonstrate a small overlap with this given state, as can be seen from Fig. 8 (c). Furthermore, we also note that the recursive quantum-HSF-induced scars²⁵ might not always show zero entanglements for cut at the center of the system; we have shown this in Appendix C within a relatively smaller fragment with $L = 14$ and $N_f = L/2 + 1$. In this fragment, the scar states exhibit zero entanglement for a cut at the site $L/2 + 2$.

As we have mentioned earlier, a recursive quantum HSF has been introduced in Ref. 25 in the East model for a longer-range variant with $r = 2$ (our model corresponds to $r = 1$). While recursively building the left-restricted part of the scar states, Ref. 25 presented a necessary condition that the expect-

tation value of n_l has to be zero where l is the rightmost site of the left-restricted part for the model with $r = 2$. However, our analysis for the $r = 1$ model demonstrates that the only necessary condition for this mechanism to occur is that the left-restricted part $|\phi'_L\rangle$ and the right-restricted part $|\phi_R\rangle$ should not interact with each other due to a blockaded region consisting of 0's residing in between the two parts whose length is $\geq (r + 1)$. In addition, the other necessary condition is the left-restricted entangled state should be the zero-energy eigenstate of the left-restricted classical fragment of the East model, as was mentioned in Ref. 25. We have explicitly verified this fact using our analytical construction. We also discuss the robustness of these scar states for different perturbations in Appendix G. In that analysis, we consider three different perturbations, namely, a random on-site potential μ_j , a random hopping J_j , and a nearest-neighbor density-density interaction V ; each of these keeps the fragmentation structure of the Hilbert space intact. We show in Appendix G that while these scar states get perturbed only gradually by the effects of μ_j and V , they vanish completely when a small random hopping is introduced.

VII. DYNAMICAL SIGNATURES OF THE LACK OF THERMALIZATION IN THE EAST MODEL

We will now discuss the dynamical signatures of the lack of thermalization due to various mechanisms, namely, the structure imposed by HSF and the presence of subspace-restricted quantum many-body scars.

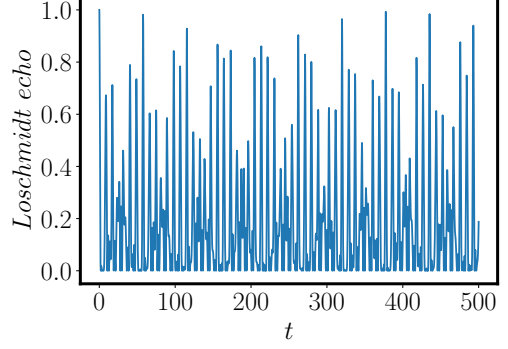
A. Dynamics due to subspace-restricted quantum many-body scars

We will start by examining the dynamical signatures of quantum many-body scars^{11,12,15,16,63} within sufficiently large non-integrable fragments. In Fig. 9 (a), we show the dynamics of the Loschmidt amplitude, given by $|\langle\psi|\psi(t)\rangle|^2$, where the initial state is taken to be

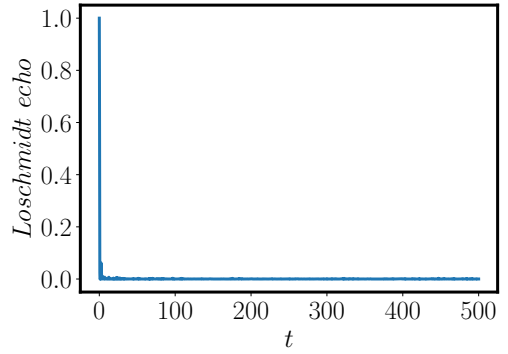
$$|\psi\rangle = \frac{1}{\sqrt{3}} (|11100110\rangle - |11010101\rangle + |10111001\rangle) \otimes |00\rangle \otimes |11111110\rangle \quad (17)$$

with which the scar eigenstates have large non-zero amplitudes. As shown in Fig. 9 (a), the Loschmidt amplitude exhibits long-time revivals; this is similar to what is seen in the case of scar states. However, it is difficult to compute the period of revival for this case since there are multiple energy scales arising from the diagonalization of this scar subspace as discussed before. As a comparison, we show in Fig. 9 (b) the dynamics starting from the root state for the same fragment, i.e., $|10 \cdots 101 \cdots 1\rangle$ which is not a part of the scar subspace; this shows a strikingly distinct behavior from Fig. 9 (a). In this case, we see that the Loschmidt echo quickly goes to zero, clearly demonstrating thermalization.

We also examine the Loschmidt echo dynamics within an-



(a)



(b)

FIG. 9: (a) Dynamics of the Loschmidt amplitude with time, starting from a basis state with which the scar eigenstates have large non-zero overlaps. We choose the initial state to have the form $|\phi_L\rangle \otimes |00\rangle \otimes |1011111\rangle$, where $|\phi_L\rangle = \frac{1}{\sqrt{3}}(|11100110\rangle - |11010101\rangle + |10111001\rangle)$. (b) Dynamics of the Loschmidt amplitude, starting from the root state of the fragment which does not have a significant overlap with the scar states. We consider the largest fragment for $L = 18$ and $N_f = L/2 + 3$ with OBC for both cases. (a) In the first case, the Loschmidt amplitude exhibits persistent oscillations for a long time; however, the amplitude never reaches unity, suggesting that these subspace-restricted scars are not perfect scars. (b) In the second case, the Loschmidt amplitude quickly decays to zero, which is a signature of thermalization within this fragment.

other comparatively smaller fragment for $L = 14$ and $N_f = 8$, starting with an initial state

$$|\psi\rangle = \frac{1}{\sqrt{3}} (|11100110\rangle - |11010101\rangle + |10111001\rangle) \otimes |00\rangle \otimes |1110\rangle. \quad (18)$$

This state has a strong overlap with the scar states within the invariant subspace discussed in Appendix C. We see perfect revivals with a period of oscillation $T = \sqrt{2}\pi$, as shown in Fig. 10. In this case, one can readily understand the period of oscillation analytically as follows. The effective Hamiltonian

within this scar subspace is given by

$$H = \begin{pmatrix} 0 & 1 & 0 \\ 1 & 0 & 1 \\ 0 & 1 & 0 \end{pmatrix}, \quad (19)$$

where the basis states in the right-restricted part are given by $|1110\rangle$, $|1101\rangle$, and $|1011\rangle$. The eigenvalues of Eq. (19) are $\sqrt{2}$, 0, and $-\sqrt{2}$, and the corresponding eigenvectors are

$$\psi_1 = \frac{1}{2} \begin{pmatrix} 1 \\ \sqrt{2} \\ 1 \end{pmatrix}, \quad \psi_2 = \frac{1}{\sqrt{2}} \begin{pmatrix} 1 \\ 0 \\ -1 \end{pmatrix}, \quad \psi_3 = \frac{1}{2} \begin{pmatrix} 1 \\ -\sqrt{2} \\ 1 \end{pmatrix}, \quad (20)$$

respectively. In terms of these three eigenstates, the time-evolved state can be recast as

$$|\psi(t)\rangle = \frac{1}{2} \left(\psi_1 e^{-i\sqrt{2}t} + \psi_3 e^{i\sqrt{2}t} + \sqrt{2}\psi_2 \right). \quad (21)$$

Hence, the Loschmidt echo as a function of t can be simplified to $\frac{1}{4} \left(\frac{3}{2} + 2 \cos(\sqrt{2}t) + \frac{1}{2} \cos(2\sqrt{2}t) \right)$ after some analytical manipulations; this expression demonstrates a perfect revival pattern with a period of oscillation given by $T = \sqrt{2}\pi$. This is exactly what we see in Fig. 10.

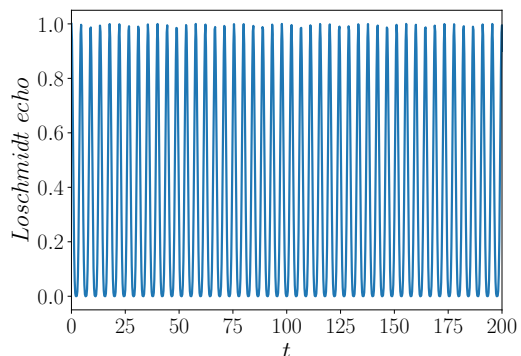


FIG. 10: Plot of the Loschmidt echo versus t for the same fragment as shown in Fig. 19. We start from an initial state with a form $|\phi_L\rangle \otimes |00\rangle \otimes |1110\rangle$, where the left-restricted part is chosen the same as in Fig. 9. This initial state has large overlaps with the scar states, which results in persistent oscillation in the dynamics with a period of oscillation $T = \sqrt{2}\pi$.

B. Anomalous behaviors of bulk and boundary autocorrelation functions due to HSF

In this section, we will demonstrate how the fragmentation structure in this model gives rise to anomalous behaviors of the bulk and boundary autocorrelation functions. This includes a non-uniform profile of the long-time saturation values of autocorrelators near the edges of the chain; this has also

been observed earlier in the literature^{20,23,39,65,66}. This behavior is more prominent in this model due to two reasons. The first one is the lack of inversion symmetry, which creates an asymmetry between the behaviors at the two boundaries (left and right), and the second is the strong-to-weak fragmentation transition³³.

To address the first question, we first examine the behavior of the unequal-time autocorrelation functions

$$C_j(t) = \langle \psi_0 | (n_j(t) - 1/2)(n_j(0) - 1/2) | \psi_0 \rangle, \quad (22)$$

starting from a random typical initial state, given by $|\psi_0\rangle = \sum_j r_j |\phi_j\rangle$, where r_j are numbers chosen from a uniform distribution in $[-1, 1]$ with zero mean (satisfying the normalization condition $\sum_j |r_j|^2 = 1$), and $|\phi_j\rangle$'s are the Fock basis states. In Figs. 11 (a-c), we plot the long-time behavior of autocorrelation functions for site $l = 2$, $l = L$, and $l = L/2$, respectively, for $L = 20$ at half-filling with OBC. In Fig. 11 (a), we observe that $C_2(t)$ oscillates around a finite value of ~ 0.17 , unlike a thermalizing system, where we expect a saturation value of $C_2(\infty) = 0$ at half-filling. (We do not study the autocorrelation $C_1(t)$ at the leftmost site since the number at that site remains frozen for all times). To analytically understand the finite saturation value of the autocorrelation function at the site $j = 2$, we consider the first three sites of an infinitely long chain undergoing transitions allowed by the East constraint; these three sites can include eight states in the number basis, 111, 110, 011, 101, 100, 010, 001, and 000. Therefore, the probability for the occurrence of each of these basis states in a typical thermal state is $1/8$ in this three-site approximation. Furthermore, the finite saturation value of the autocorrelator at $j = 2$ can be supported by those states out of these eight states, which remain dynamically frozen at the site $j = 2$, regardless of the occupation numbers on any other sites of the chain. Taking this fact into consideration, we see that only five states, i.e., 000, 001, 100, 010, and 011 host dynamical frozen configuration at $j = 2$. This gives a saturation value equal to $1/8 \times 1/4 \times 5 \simeq 0.156$, which is quite close to our numerically obtained mean saturation value. However, the other boundary in the East model behaves in a completely distinct manner, as shown in Fig. 11 (b), due to the lack of inversion symmetry. In this case, we see that $C_L(t)$ initially shows a sharp transient decay; following this, it gradually decays to a finite saturation value of about 0.09 around which it oscillates at long times. The saturation value at the rightmost site, $C_L(\infty)$, is much smaller than at the leftmost site. In Fig. 11 (c), we demonstrate the behavior of the autocorrelation function inside the bulk, $C_{L/2}(t)$, which again shows a decay profile similar to the rightmost site. However, the long-time saturation value of ~ 0.05 for this case is smaller compared to the two boundary sites, but it is clearly positive unlike a thermalizing system. This thus suggests that apart from distinct bulk and boundary profiles of autocorrelators, which are typically observed in fragmented systems, the two boundaries also illustrate quite different features due to the lack of inversion symmetry in this model; to the best of our knowledge, this feature has not been observed in any other models in the context of HSF.

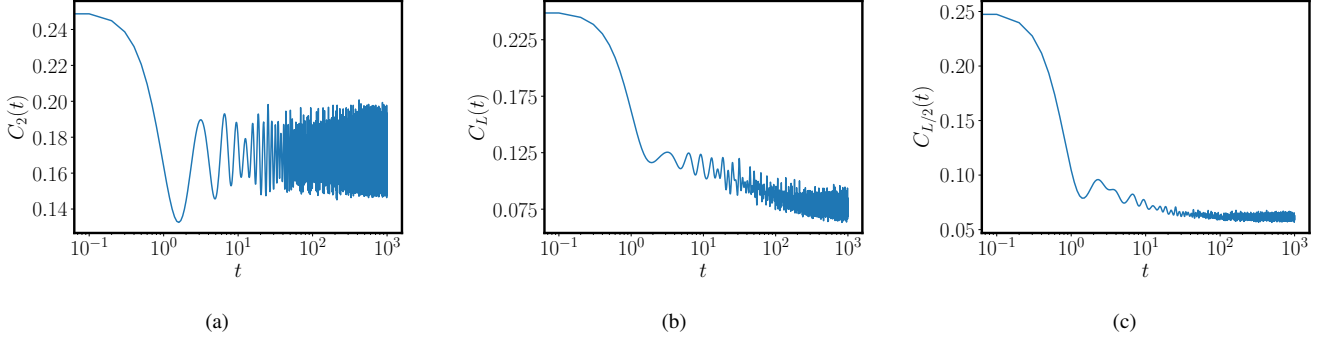


FIG. 11: (a-c) Plots depicting the behaviors of C_2 , C_L and $C_{L/2}$ with t starting from a random initial state. (a) $C_2(t)$ oscillates around a finite saturation value (~ 0.17) at long times. (b) The right boundary site, $C_L(t)$, demonstrates a distinct behavior from C_2 . We see a gradual decay to a saturation value (~ 0.09) which is much smaller compared to the left boundary site. This is a signature of broken inversion symmetry. (c) The autocorrelation in the bulk, $C_{L/2}(t)$, depicts a similar behavior as $C_L(t)$. However, the saturation value (~ 0.05) is much smaller compared to the two boundary sites.

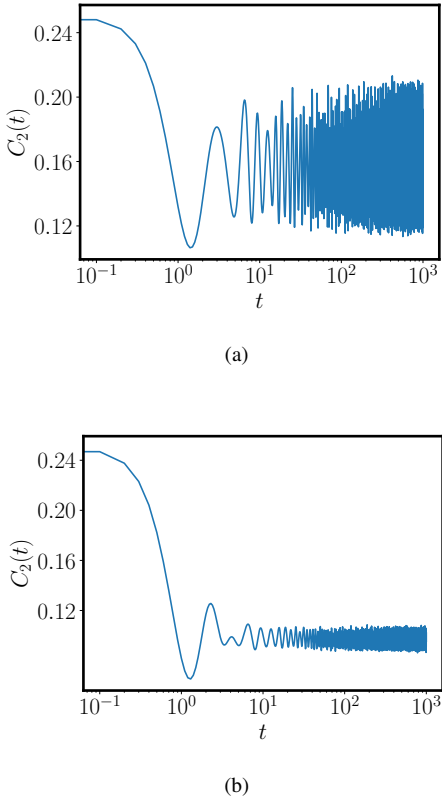


FIG. 12: (a-b) The behavior of $C_2(t)$ with t starting from a random initial state for $L = 20$ for $N_f = L/2 - 2$ and $L/2 + 3$, respectively, with OBC. $C_2(t)$ for the first case oscillates around a saturation value (~ 0.16), which is much larger than the value found in the latter case (~ 0.1). These two distinct behaviors of long-time saturation value of left boundary autocorrelators again illustrate that there is a transition from the strong-to-weak fragmentation as one moves from below to above half-filling in this model.

To address the second question related to the strong-to-weak fragmentation as the filling is varied, we examine the boundary autocorrelation function $C_2(t)$ below and above half-filling for a system with $L = 20$, for $N_f = L/2 - 2$ and $N_f = L/2 + 3$, respectively. This is shown in Figs. 12 (a-b). In both cases, the initial state is chosen to be a typical random initial state, similar to the one considered in Fig. 11. Furthermore, the filling above half-filling, $N_f = L/2 + 3$, is chosen such that the largest fragment within the full Hilbert space for $L = 20$ lies at this filling. As demonstrated in Figs. 12 (a-b), the different fragmentation structures have a profound effect on the long-time saturation values of the boundary autocorrelators below and above half-filling. In Fig. 12 (a), we see that the saturation value (~ 0.16) about which $C_2(t)$ oscillates around is much larger than the case above half-filling (~ 0.1) which is shown in Fig. 12 (b). The larger saturation value of C_2 is purely a manifestation of the strong fragmentation structure, where the largest fragment growth is exponentially smaller than the full Hilbert space size, while in the latter case, the growth of the largest fragment is the same as that of the full Hilbert space (up to powers of L). Another remarkable thing to note is that the Hilbert space size for the first case is 125970, whereas in the second case, the Hilbert space size is 38760. It is generally observed that the amplitude of late-time oscillations becomes more sharply well-defined with increasing system sizes; however, we see exactly the opposite feature in our model. This suggests that there are exponentially many disconnected fragments which govern the long-time behavior of $C_2(t)$. In addition, the amplitude of oscillations in the first case being much larger than in the second case again confirms that the dimension of the largest fragment is exponentially smaller than the full Hilbert space size.

VIII. EFFECTS OF NEAREST-NEIGHBOR DENSITY-DENSITY INTERACTIONS WITH FINITE STRENGTH

The robustness of the fragmentation structure under perturbations^{67–69} is, in general, an interesting question to address and has been studied extensively in recent times. The rich behavior of the fragmentation structure in the East model, namely, weak and strong fragmentation for different fillings³³, and several fragmentation-induced anomalous properties²⁵ (for instance, the filling fraction for the ground state shifting with the system size, and the presence of quantum many-body scars within different fragments) motivates us to examine the effects of perturbations in this model. In this direction, a commonly studied perturbation, which can be realized in various experimental platforms^{1–4} (for instance, the Rydberg blockade limit of a Rydberg simulator) is a uniform nearest-neighbor density-density interaction with strength V . As we will discuss below, this perturbation can give rise to some intriguing features in this fragmented system.

A. Effects of finite- V on the ground state properties

The model under consideration has the Hamiltonian

$$H = \sum_j n_{j-1} (c_j^\dagger c_{j+1} + \text{H.c.}) + V \sum_j n_j n_{j+1}, \quad (23)$$

where V is the strength of the nearest-neighbor density-density interaction. We note that an interaction with a finite strength does not change the fragmentation structure of the East model because it is diagonal in the number basis. However, we will see later that taking the limit $V \rightarrow \infty$ drastically changes the fragmentation structure of the model. We will first study the effects of a finite V on the ground state properties of the model. We have seen earlier that the East model without interactions has some unusual properties for the ground state, namely, the filling for the ground state shifts with increasing system sizes, as shown in Fig. 3. However, we find that shift in the ground state filling becomes stabilized at half-filling after a threshold value of V . In Fig. 13, we show the ground state energy versus filling for $L = 20$ with PBC for several values of V . We note that the ground state energy shifts towards half-filling as V increases; eventually it stabilizes at half-filling. The reason for the stabilization of the ground state at half-filling can be qualitatively understood as follows. Although interactions with finite V do not change the fragmentation structure, it introduces a large energy cost for those configurations of states where two or more fermions sit next to each other. Hence, the configurations that are energetically favorable typically lie at half-filling or below half-filling. On the other hand, the natural tendency of the fragmentation structure due to the East constraint is to give rise to the largest fragment away from half-filling, and such a fragment typically favors the ground state due to its larger size compared to others; this pushes the ground state away from half-filling. The

energy cost due to finite- V therefore competes with the fragmentation structure imposed by the East constraint. These opposing proclivities eventually brings the ground state towards half-filling with increasing V , and it finally stabilizes at half-filling after a threshold strength of V .

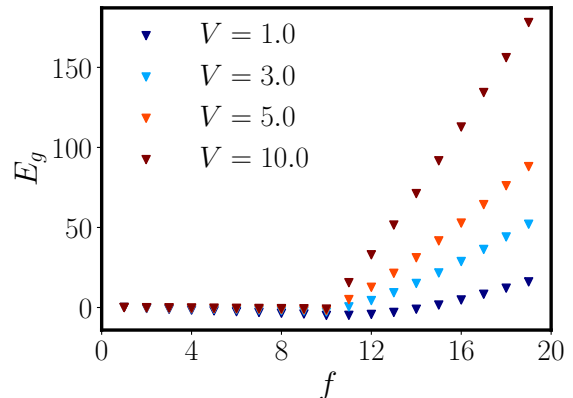


FIG. 13: Plot showing the ground state energy as a function of filling for the East model with a density-density interaction for several values of V , for $L = 20$ with PBC. Contrary to Fig. 3 which corresponds to the East model with $V = 0$, the ground state for the interacting system stabilizes at $N_f = L/2$ beyond a threshold value of V .

B. Effects of finite- V on the thermalization properties

We will now describe how the thermalization properties of the East model change as the interaction strength is increased. To do this analysis, we restrict ourselves to the largest fragment of the East model, which remains unchanged in the presence of a finite V . In Figs. 14 (a-c), we show the level spacing distributions of consecutive energy levels within the largest fragments for several values of $V = 0$ (the original East model), 3 and 5, for $L = 18$ and $N_f = L/2 + 3$ (this fragment has 9996 states). As we have discussed before, the largest fragment of the East model follows the GOE statistics^{47–49} with $\langle \tilde{r} \rangle = 0.5298$ (close to the GOE value), as shown in Fig. 14 (a). However, the level spacing distribution shows a transition from the GOE^{47–49} to the Poisson distribution^{47,48,57} as V increases. In Figs. 14 (b-c), we show a similar analysis for $V = 3$ and $V = 5$, which have $\langle \tilde{r} \rangle \simeq 0.503$ and $\langle \tilde{r} \rangle \simeq 0.417$ (close to the Poisson value), respectively. This emergent Poisson statistics with increasing V is due to the statistical bubble localization^{52,53} within the largest fragment, which causes a breakdown of the subspace-restricted ETH. The reason for this is that increasing V introduces a large energy cost for certain configurations where two or more nearest-neighbor sites are occupied; this gives rise to a secondary fragmentation within a primary fully connected fragment by generating some emergent approximate conserved quantities. The “bubble-neck” structures of the

eigenstates in the bubble localized phase^{52,53}, therefore, split up the active region into many subsectors, and the lack of level repulsion between these subsectors finally produces the Poisson level statistics^{47,48,57}. Further, the entanglement entropy is no longer a smooth function of the energy as shown in Fig. 15 (a).

In the next section, we will study the limit $V \rightarrow \infty$ limit and show that this leads to a constraint-integrable model^{24,54}.

IX. EAST MODEL WITH DENSITY-DENSITY INTERACTIONS IN THE INFINITE- V LIMIT

We will now examine the model given in Eq. (23) in the limit $V \rightarrow \infty$. The effective Hamiltonian in this limit can be obtained by comparing the energy cost on the two sides of the allowed transitions. To find the effective Hamiltonian, we note that the East transitions can be recast involving four consecutive sites, as (i) $1100 \leftrightarrow 1010$ and (ii) $1101 \leftrightarrow 1011$. Although the original East transitions involve only three consecutive sites, the computation of the energy cost due to the V term demands the consideration of these four-site configurations. The energy costs on the two sides of the above transitions are as follows: (i) V (left side) and 0 (right side), and (ii) V (left side) and V (right side). Hence only the second transition (in which the two sides have the same energy cost) is allowed in the limit $V \rightarrow \infty$. This gives rise to the following Hamiltonian involving four consecutive sites,

$$H = \sum_j n_{j-1} \left(c_j^\dagger c_{j+1} + \text{H.c.} \right) n_{j+2}. \quad (24)$$

Eq. (24) describes a correlated-hopping model, where a nearest-neighbor hopping is allowed only when the sites to their left and right are both occupied. Following a Jordan-Wigner transformation from spinless fermions to spin-1/2's, the model is described by a spin Hamiltonian of the form

$$H = \sum_j P_{j-1} \left(\sigma_j^x \sigma_{j+1}^x + \sigma_j^y \sigma_{j+1}^y \right) P_{j+2}, \quad (25)$$

where $P_j = (1 + \sigma_j^z)/2$ projects on to a state with \uparrow spin on the j -th site, and $\sigma_j^x, \sigma_j^y, \sigma_j^z$ denote the Pauli matrices. This model can thus be called the PXXP+PYYP model³⁴. Since this model only allows the transitions $1101 \leftrightarrow 1011$, it can be considered to be one-half of the folded-XXZ model^{24,34} which allows both $1101 \leftrightarrow 1011$ and $0100 \leftrightarrow 0010$. Surprisingly, the PXXP+PYYP model is invariant under spatial inversion, unlike the East model with $V = 0$. We will now discuss the fragmentation structure and other features of this model in detail in the next section.

A. Characterization of root states

We will first elucidate how to label each fragment in this model by a unique root state, similar to the East model discussed Sec. III A. In doing so, we utilize a similar procedure

as discussed before, i.e., we will bring all the configurations appearing within a particular fragment to a uniquely defined root configuration having a simple form. This identification will enable us to determine all the root states for the different fragments. We now note that there are two alternative ways to define the root states here since this model is inversion symmetric, unlike the East model where there is only one way to specify the root states due to the lack of inversion symmetry. Out of these two ways, we will use the root identification procedure which is similar to the East model. To begin with, it can be checked that all the states within a simple and fully connected fragment can be reduced to a unique root state by moving all pairs of 10's to the leftmost side of the string while successively removing all 1101's. This generates the form $\psi_L \otimes \psi_m \otimes \psi_R$, where ψ_L is either ϕ or has only 0's, ψ_m has only 10's, and ψ_R is either ϕ , all 0's or 0's followed by 1's, or all 1's. We will now discuss the rules to determine the sizes of the fragments.

(i) We can check that ψ_L never participates in the dynamics, and therefore it should be removed from the computation of the dimensions of the different fragments.

(ii) In addition, if ψ_R is ϕ , 0's or 0's followed by 1's, then ψ_R should also be removed from the calculation of the dimensions of fragments; such root states constitute class I. But if when ψ_R comprise 1's, such 1's should be integrated into the counting process, and consequently, such root states comprise class II.

After specifying these rules, we further note that the pairs of 10's always hop as a unit within a specific fragment. In addition, the rightmost 1 for all the configurations within fragments falling under class II, i.e., ψ_R comprising 1's, always remains dynamically inactive. However, its presence is essential for the facilitated hopping processes allowed by this model. Accordingly, this 1 should also be removed from the calculation of the dimensions of such fragments. Next, we denote the number of 10's and 1's in ψ_m and ψ_R as N_A and N_B , respectively. With these rules, the dimension of a fully connected fragments is found to be

$$D(L) = \frac{(N_A + N_B - 1)!}{N_A!(N_B - 1)!}, \quad (26)$$

where $L = 2N_A + N_B$, and the filling fraction is $f = \frac{N_A + N_B}{L}$ provided that ψ_L is ϕ .

We can generalize these rules to compute the dimensions of more complicated fragments where there are multiple dynamically active regions separated from each other by inactive blockade configurations. For such fragments, the most general root state takes the separable form $\psi_L \otimes \psi_{B_1} \otimes \psi_{I_1} \otimes \psi_{B_2} \otimes \psi_{I_2} \cdots \otimes \psi_{I_n} \otimes \psi_{B_n}$, where ψ_L is ϕ or all 0's, and ψ_{I_i} has all 0's (2 or more in number). In addition, ψ_{B_i} (except the rightmost one) can be further divided into two blocks $\psi_{m_i} \otimes \psi_{R_i}$, where ψ_{m_i} consists of pairs of 10's, and ψ_{R_i} contains ϕ or 0's followed by 1's or all 1's. Further, the rightmost ψ_{B_n} again consists of two parts, ψ_{m_n} and ψ_{R_n} , where ψ_{m_n} is 10's, and ψ_{R_n} contains either ϕ , all 0's, 0's followed by 1's or all 1's. We should again note that ψ_L never participates in the dynamics, and the role of ψ_{I_i} is to keep the active re-

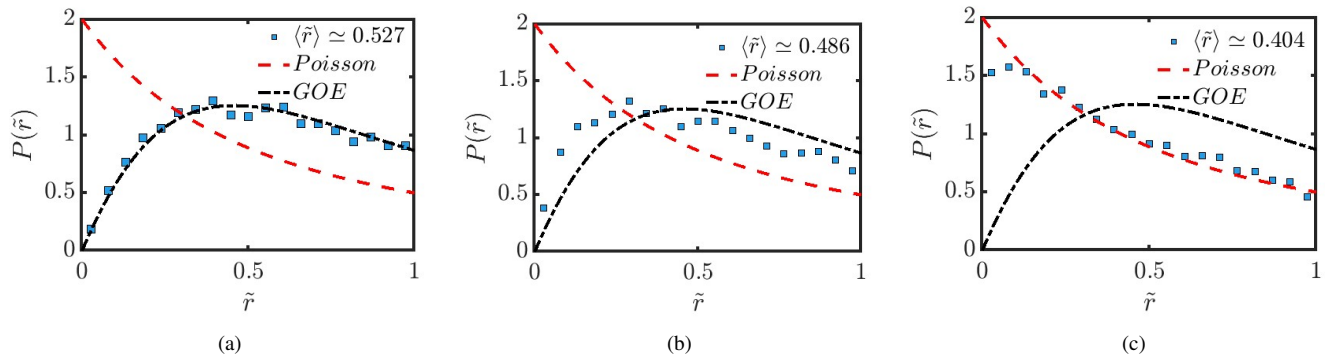


FIG. 14: (a-c) Plots showing the level spacing statistics between consecutive level ratios for $V = 0, 3$, and 5 , respectively, within the largest fragment for $L = 18$ and $N_f = L/2 + 3$ (the fragment size is 9996). The value of $\langle \tilde{r} \rangle$ shows a transition from the GOE to the Poisson distribution with increasing V , namely, $\langle \tilde{r} \rangle \sim 0.527$ (the GOE value), 0.486 and 0.404 (close to the Poisson value) for $V = 0, 3$ and 5 , respectively, as illustrated in plots (a-c). The distribution of level spacing ratios indicates that there is a transition occurring from non-integrability (subspace-restricted thermalization) to integrability (statistical bubble localized phase) within the largest fragment as V increases.

gions given by ψ_{B_i} dynamically separated from each other. These blocks, thus, do not play any active role in counting the dimensions of fragments. The ψ_{B_i} 's are therefore independent and fully connected dynamically active fragments which remain isolated from each other due to the presence of blocked regions. The dimension of such generalized fragments can, therefore, be obtained by taking a product of the dimensions of each active region given by the rules discussed earlier. We thus obtain the general expression

$$D_{\text{gen}}(L) = \prod_{i=1}^n \frac{(N_{A_i} + N_{B_i} - 1)!}{N_{A_i}!(N_{B_i} - 1)!}, \quad (27)$$

where N_{A_i} and N_{B_i} are the number of 10's and 1's in ψ_{m_i} and ψ_{R_i} , which form a block ψ_{B_i} .

B. Number of fragments in the PXXP+PYYP model

We will now count the number of fragments in this model with OBC using the transfer matrix method, similar to the procedure discussed for the East model^{25,33}. We note that identifying the root configuration for each fragment requires us to remove all occurrence of 1101's; hence the resultant transfer matrix^{28-31,45}, T_3 should not allow any occurrences of 1101. Using this fact, a transfer matrix computation shows that N_{frag} in this model grows asymptotically as 1.867^L ; we have also confirmed this numerically. The details of the transfer matrix computation are shown in Appendix D.

We note that the number of fragments in this model grows much faster with L compared to the East model. This is understandable since the infinite- V limit forbids more transitions than the East model. Hence the degree of fragmentation in the infinite- V model is higher than in the East model.

We can again count the total number of fragments N_{frag} for a given system size L with OBC by using the fact that $N_{frag} = \sum_{i,j} M_{i,j}$ where $M = T_3^{L-3}$. The number of fragments for the first few values of L is shown in Table III; we

find that these agree with our numerical results. In addition, we have $N_{frag}(L) = 1, 2$ and 4 for $L = 0, 1$ and 2 , respectively.

L	3	4	5	6	7	8	9	10
N_{frag}	8	15	28	52	97	181	338	631

TABLE III: N_{frag} versus L .

We also note from Table III that N_{frag} follows recursion relation

$$N_{frag}(L) = N_{frag}(L-4) - N_{frag}(L-3) + 2N_{frag}(L-1), \quad (28)$$

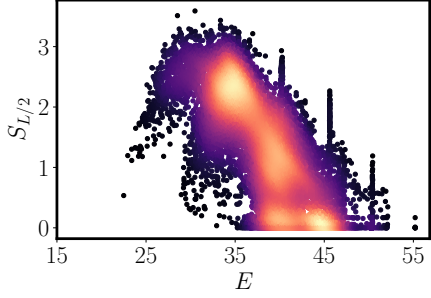
for $L \geq 4$.

C. Frozen fragments in the PXXP+PYYP model

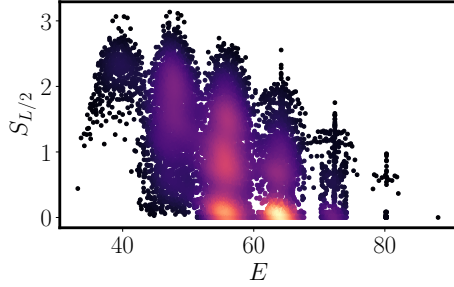
We will now find the growth with system size of the number of frozen eigenstates in the PXXP+PYYP model using a similar transfer matrix method. Since these eigenstates are completely inactive dynamically, the counting of such states requires us to remove both 1101 and 1011 from the transfer matrix construction. Then one finds that the number of fragments N_{froz} grows as 1.8124^L for a system with OBC; we have verified this numerically. The details of the transfer matrix calculation^{28-31,45} are shown in Appendix E. We again see that N_{froz} in this model grows faster than in the East model; this is due to the fact that the infinite- V model forbids some processes which are allowed in the East model with $V = 0$.

D. Description of the largest fragment

We will now compute the dimension of the largest fragment to get more insight into the fragmentation structure of



(a)



(b)

FIG. 15: (a-b) Plots showing the spectrum of $S_{L/2}$ versus E for $V = 5$ and $V = 8$ in the largest fragment for $L = 18$ and $N = L/2 + 3$. Both these plots demonstrate that $S_{L/2}$ is not a smooth function of E due to an emergent statistical bubble localization. This emergent bubble localization further causes secondary fragmentation within a primary fragment; this is distinctly visible in the entanglement spectrum as we see in Fig. (b) for $V = 8$.

this model. We have shown in Sec. IX A that the dimension of a simple and fully connected fragment specified by a root state $\psi_L \otimes \psi_m \otimes \psi_R$ is given by

$$D^{PXXP}(L) = \frac{(N_A + N_B - 1)!}{N_A!(N_B - 1)!}, \quad (29)$$

where N_A and N_B are the total number of 10's and 1's in ψ_m and ψ_R , respectively. For simplicity, let us now assume that ψ_L is ϕ ; this allows us to use the relations $L = 2N_A + N_B$ and filling $f = N_A + N_B$. To study the thermodynamic limit $L \rightarrow \infty$, we parameterize $N_A = \alpha L$ and $N_B = \gamma L$, where $\alpha, \gamma \geq 0$. These parameters satisfy $2\alpha + \gamma = 1$ and $f = (1 - \alpha)L$. After using Stirling's approximation, Eq. (29) simplifies to

$$D(L) = \left(\frac{(1 - \alpha)^{1-\alpha}}{\alpha^\alpha (1 - 2\alpha)^{1-2\alpha}} \right)^L, \quad (30)$$

where we set $\gamma = 1 - 2\alpha$. Extremizing the Eq. (30) with respect to α , we find that the dimension of the largest fragment in the thermodynamic limit occurs at $\alpha = \frac{1}{2} \left(1 - \frac{1}{\sqrt{5}} \right) \simeq$

0.276. The filling f for the largest fragment is then given by $(1 - \alpha)L \simeq 0.724 L$. Strikingly, the dimension of the largest fragment then turns out to be 1.618^L , which is exponentially smaller than the full Hilbert space size of 2^L . Hence this model exhibits strong fragmentation^{11,31}, unlike the East model, where we observe weak fragmentation at this filling which lies above half-filling.

E. Integrability of the PXXP+PYYP model and ground state analysis

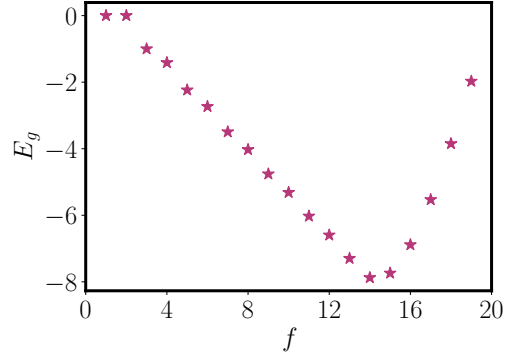


FIG. 16: Plot showing the ground state energy E_{GS} versus the filling N_f for the PXXP+PYYP model for $L = 20$ with OBC. We see that the ground state appears at $N_f = 14$, which means the filling fraction is $\rho = 0.7$. This is close to the value of 0.699 which is predicted analytically in the thermodynamic limit.

We will now argue that PXXP+PYYP falls under the class of constraint-integrable model^{24,54}, in contrast to the East model which is non-integrable^{25,33}. To prove the integrability of this model, we map each fragment to a non-interacting tight-binding model of spinless fermions with nearest-neighbor hopping on a system with OBC. This can be accomplished by noting that facilitated hopping in this model always makes a pair of 10 hop as a unit. Accordingly, there are effectively two degrees of freedom available during the transitions, which are 10's and 1's. This allows us to map 10 and 1 to a hole and a particle, given by $|0\rangle$ and $|1\rangle$, respectively. Following this mapping, we see that the model within each connected fragment simply reduces to a nearest-neighbor tight-binding model of spinless fermions, where the energy spectrum $E = \sum_n E_n$, where the single-particle energies are given by

$$E_n = -2 \cos \left(\frac{\pi n}{N_A + N_B} \right), \quad (31)$$

with $n = 1, \dots, N_A + N_B - 1$. To find the total energy E , all possible combinations of n 's have to be taken into account, with the number of n 's within a given fragment being given by $N_B - 1$. Here, N_A and N_B define the number of 10's and 1's in the parts ψ_m and ψ_R of the root state; al-

ternatively, these give the total numbers of 0's and 1's in the mapped model. We also note that the rightmost $|1\rangle$ never participates in the hopping process for this newly mapped tight-binding model of length $L' = N_A + N_B$. This fact, along with the OBC, makes the single-particle dispersion different from a tight-binding model with PBC. The single-particle dispersion in Eq. (31) can be obtained by observing that the single-particle wave function at site j in state n is given by $\psi_n(j) = \sin\left(\frac{\pi n j}{N_A + N_B}\right)$, which follows from the hard-wall boundary condition $\psi_n(0) = \psi_n(L' = N_A + N_B) = 0$. We remark here that the integrability of the PXXP+PYYP model has been discussed recently using the Bethe Ansatz in Ref. 54; however, our mapping of this model to a nearest-neighbor tight-binding model of non-interacting fermions within each fragment explains the integrability very easily.

Having discussed the integrability of the PXXP+PYYP model, we will now compute the filling fraction at which the ground state of the model appears. An analytical computation presented in Appendix F shows that in the thermodynamic limit, the filling fraction at which the ground state lies is given by $\rho \simeq \pi/4.493 = 0.699$, and the ground state energy is $E_{GS} \simeq 0.435L$. We numerically validate this result by studying the ground state of the PXXP+PYYP model for $L = 20$ as a function of the filling f . This shows that the ground state lies at a filling, $f = 14$. This implies $\rho = 0.7$ which is very close to the analytically predicted value of $\rho \simeq 0.699$. This agrees with our numerical results; see Fig. 16. Surprisingly, we see that the ground state in this model lies at a filling fraction which is less than the filling fraction 0.724 where this model has the largest fragment in the thermodynamic limit. This anomalous behavior is in contrast to what we found in the East model; there the ground state lies in the largest fragment, and the filling fraction for the ground state shifts away half-filling with increasing system size.

F. Experimentally realizable models

We will discuss here how to experimentally realize the PXXP+PYYP model involving terms with four consecutive

sites by considering a particular limit of the $t - V$ model (a model of spinless fermions which has a nearest-neighbor hopping and a nearest-neighbor density-density interaction with strength V), which has a specific pattern of on-site potentials pattern³¹. We consider the Hamiltonian

$$H_4 = \sum_j [c_j^\dagger c_{j+1} + c_{j+1}^\dagger c_j + V_j (2n_j - 1)(2n_{j+1} - 1) + \mu_j(2n_j - 1)], \quad (32)$$

where V_j varies with j with period four, namely, $V_{4j+1} = V_1$, $V_{4j+2} = V_2$, $V_{4j+3} = V_3$, and $V_{4j+4} = V_4$. Similarly, μ_j also has a spatial periodicity of four sites such that $\mu_{4j+1} = \mu_1$, $\mu_{4j+2} = \mu_2$, $\mu_{4j+3} = \mu_3$ and $\mu_{4j+4} = \mu_4$. We have set the strength of the nearest-neighbor hopping to be unity for convenience. We now consider all possible correlated-hopping processes involving four consecutive sites, namely, $1101 \leftrightarrow 1011$, $0100 \leftrightarrow 0010$, $1100 \leftrightarrow 1010$ and $0101 \leftrightarrow 0011$, for all the possible patterns of the interactions and on-site potentials. We will compare the energy cost on both sides of the different transitions mentioned above for $V_1, V_2, V_3, V_4 \rightarrow \infty$, and $\mu_1, \mu_2, \mu_3, \mu_4 \rightarrow \infty$, as shown in Table IV; this will allow us to find an effective Hamiltonian in the limit of large interaction strengths and on-site potentials. The table shows that the energy costs on the left and right sides of the correlated-hopping process $1101 \leftrightarrow 1011$ are equal to each other provided $V_1 = -V_3 = V_2 = V_4 = V$ with $\mu_3 = \mu_4 = -\mu_1 = -\mu_2 = V$. However, these parameter values do not support the other three correlated-hopping processes in the $V \rightarrow \infty$ limit as the energy costs on the two sides of these processes differ by infinitely large amounts. Hence we see that an experimentally realizable $t - V$ model with a special pattern of large nearest-neighbor interactions and on-site potentials μ_j reduces to the PXXP+PYYP model.

X. DISCUSSION

We will now summarize the main results obtained in this paper. We have studied a particle-number conserving quantum East model^{25,33}, which only allows nearest-neighbor hoppings between sites j and $j + 1$ when the neighboring site $j - 1$ is occupied. This model is known to exhibit a filling-dependent weak-to-strong fragmentation transition^{32,33}. To unravel the fragmentation structure, we have presented an alternative formalism based on the identification of the canonical representation of the root states which define each fragment^{42,43}. This root identification procedure enables us to

uncover various aspects of the fragmented Hilbert space in this model, namely, the total number of fragments, the number of frozen eigenstates, and the dimension of the largest fragment, using the transfer matrix and enumerative combinatorics methods^{28-31,45}. In addition, the growth of all the fragments in this model can be captured by using the appropriate Dyck word sequences⁴⁶. Our analysis further revealed that the filling fraction for the appearance of the ground state and of the largest fragment shifts away from half-filling as $\sqrt{L}/2$ asymptotically; this is a consequence of the distinctive fragmentation structure of this model in terms of Dyck sequence⁴⁶.

Pattern of V_j	Pattern of μ_j	Correlated-hopping process	Energy cost for left hand side of the process in the third column	Energy cost for right hand side of the process in the third column
$V_1 V_2 V_3 V_4$	$\mu_1 \mu_2 \mu_3 \mu_4$	1101 \leftrightarrow 1011	$V_1 - V_2 - V_3 + \mu_1 + \mu_2 - \mu_3 + \mu_4$	$-V_1 - V_2 + V_3 + \mu_1 - \mu_2 + \mu_3 + \mu_4$
$V_1 V_2 V_3 V_4$	$\mu_1 \mu_2 \mu_3 \mu_4$	0100 \leftrightarrow 0010	$-V_1 - V_2 + V_3 - \mu_1 + \mu_2 - \mu_3 - \mu_4$	$V_1 - V_2 - V_3 - \mu_1 - \mu_2 + \mu_3 - \mu_4$
$V_1 V_2 V_3 V_4$	$\mu_1 \mu_2 \mu_3 \mu_4$	1100 \leftrightarrow 1010	$V_1 - V_2 + V_3 + \mu_1 + \mu_2 - \mu_3 - \mu_4$	$-V_1 - V_2 - V_3 + \mu_1 - \mu_2 + \mu_3 - \mu_4$
$V_1 V_2 V_3 V_4$	$\mu_1 \mu_2 \mu_3 \mu_4$	0101 \leftrightarrow 0011	$-V_1 - V_2 - V_3 - \mu_1 + \mu_2 - \mu_3 + \mu_4$	$V_1 - V_2 + V_3 - \mu_1 - \mu_2 + \mu_3 + \mu_4$
$V_2 V_3 V_4 V_1$	$\mu_2 \mu_3 \mu_4 \mu_1$	1101 \leftrightarrow 1011	$V_2 - V_3 - V_4 + \mu_2 + \mu_3 - \mu_4 + \mu_1$	$-V_2 - V_3 + V_4 + \mu_2 - \mu_3 + \mu_4 + \mu_1$
$V_2 V_3 V_4 V_1$	$\mu_2 \mu_3 \mu_4 \mu_1$	0100 \leftrightarrow 0010	$-V_2 - V_3 + V_4 - \mu_2 + \mu_3 - \mu_4 - \mu_1$	$V_2 - V_3 - V_4 - \mu_2 - \mu_3 + \mu_4 - \mu_1$
$V_2 V_3 V_4 V_1$	$\mu_2 \mu_3 \mu_4 \mu_1$	1100 \leftrightarrow 1010	$V_2 - V_3 + V_4 + \mu_2 + \mu_3 - \mu_4 - \mu_1$	$-V_2 - V_3 - V_4 + \mu_2 - \mu_3 + \mu_4 - \mu_1$
$V_2 V_3 V_4 V_1$	$\mu_2 \mu_3 \mu_4 \mu_1$	0101 \leftrightarrow 0011	$-V_2 - V_3 - V_4 - \mu_2 + \mu_3 - \mu_4 + \mu_1$	$V_2 - V_3 + V_4 - \mu_2 - \mu_3 + \mu_4 + \mu_1$
$V_3 V_4 V_1 V_2$	$\mu_3 \mu_4 \mu_1 \mu_2$	1101 \leftrightarrow 1011	$V_3 - V_4 - V_1 + \mu_3 + \mu_4 - \mu_1 + \mu_2$	$-V_3 - V_4 + V_1 + \mu_3 - \mu_4 + \mu_1 + \mu_2$
$V_3 V_4 V_1 V_2$	$\mu_3 \mu_4 \mu_1 \mu_2$	0100 \leftrightarrow 0010	$-V_3 - V_4 + V_1 - \mu_3 + \mu_4 - \mu_1 - \mu_2$	$V_3 - V_4 - V_1 - \mu_3 - \mu_4 + \mu_1 - \mu_2$
$V_3 V_4 V_1 V_2$	$\mu_3 \mu_4 \mu_1 \mu_2$	1100 \leftrightarrow 1010	$V_3 - V_4 + V_1 + \mu_3 + \mu_4 - \mu_1 - \mu_2$	$-V_3 - V_4 - V_1 + \mu_3 - \mu_4 + \mu_1 - \mu_2$
$V_3 V_4 V_1 V_2$	$\mu_3 \mu_4 \mu_1 \mu_2$	0101 \leftrightarrow 0011	$-V_3 - V_4 - V_1 - \mu_3 + \mu_4 - \mu_1 + \mu_2$	$V_3 - V_4 + V_1 - \mu_3 - \mu_4 + \mu_1 + \mu_2$
$V_4 V_1 V_2 V_3$	$\mu_4 \mu_1 \mu_2 \mu_3$	1101 \leftrightarrow 1011	$V_4 - V_1 - V_2 + \mu_4 + \mu_1 - \mu_2 + \mu_3$	$-V_4 - V_1 + V_2 + \mu_4 - \mu_1 + \mu_2 + \mu_3$
$V_4 V_1 V_2 V_3$	$\mu_4 \mu_1 \mu_2 \mu_3$	0100 \leftrightarrow 0010	$-V_4 - V_1 + V_2 - \mu_4 + \mu_1 - \mu_2 - \mu_3$	$V_4 - V_1 - V_2 - \mu_4 - \mu_1 + \mu_2 - \mu_3$
$V_4 V_1 V_2 V_3$	$\mu_4 \mu_1 \mu_2 \mu_3$	1100 \leftrightarrow 1010	$V_4 - V_1 + V_2 + \mu_4 + \mu_1 - \mu_2 - \mu_3$	$-V_4 - V_1 - V_2 + \mu_4 - \mu_1 + \mu_2 - \mu_3$
$V_4 V_1 V_2 V_3$	$\mu_4 \mu_1 \mu_2 \mu_3$	0101 \leftrightarrow 0011	$-V_4 - V_1 - V_2 - \mu_4 + \mu_1 - \mu_2 + \mu_3$	$V_4 - V_1 + V_2 - \mu_4 - \mu_1 + \mu_2 + \mu_3$

TABLE IV: Energy costs arising from the V_j and μ_j terms in Eq. (32) for the left and right hand sides of various correlated-hopping processes for all four sets of patterns of V_j and μ_j which are connected to one another through translation by one site, in the limit $V_1, V_2, V_3, V_4 \rightarrow \infty$ and $\mu_1, \mu_2, \mu_3, \mu_4 \rightarrow \infty$.

Next, we have studied the static and dynamic signatures of the lack of thermalization^{11,20,31} which occurs in this model due to the HSF. Our analysis of energy level spacing correlation^{47,48} reveals that although the ETH⁶⁻¹² is strongly violated within the full Hilbert space, a weaker version of the Krylov-restricted ETH¹¹ is satisfied within all sufficiently large fragments. The weaker violation of the ETH within the different fragments is supported by the presence of subspace-restricted quantum many-body scars^{20,25,50,51}, which are a consequence of the recursive quantum HSF²⁵. We then examined various measures of the ETH violation^{11,12} in the scar subspaces, such as long-time revivals in the Loschmidt amplitude, abrupt jumps in the overlap amplitudes for the scar states, and some of the few-body observables not behaving as smooth functions of the energy. We also studied the anomalous long-time behaviors of the bulk and boundary autocorrelators starting from a random initial state^{20,39,65}; these are a hallmarks of typical fragmented systems. We found that the two boundaries in the East model behave in distinct manners due to the lack of spatial inversion symmetry in this model.

We have then studied the effects of nearest-neighbor density-density interactions with strength V on the East model²⁵; this perturbation keeps the fragmentation structure of the model intact. The introduction of a finite V has a number of effects on the ground state and on the ETH properties of the system. To be specific, increasing the value of V gradually moves the ground state closer to half-filling and also induces a spectral transition from the GOE statistics (weakly ETH violating^{20,25}) to the Poisson statistics (statistical bubble localized phase^{52,53}) within sufficiently large fragments. The infinite- V limit gives a significantly different model, namely, it turns into

a constraint-integrable model^{24,54} called the PXXP+PYYP model. The integrability of this model can be readily seen by mapping it to a non-interacting nearest-neighbor tight-binding model of spinless fermions within each fragment. We have then unravelled the distinct fragmentation structure and anomalous ground state properties with the help of this mapped model. Finally, we have concluded by proposing an experimentally realizable special kind of $t - V$ model with a specific pattern of nearest-neighbor interactions and on-site potentials μ ³¹ which reduces to the PXXP+PYYP model in a particular limit.

We end by proposing possible future avenues of research. It would be worthwhile to completely characterize the classical fragmentation structure of the families of longer-range facilitated East models²⁵, which have not been explored much until now. A more detailed analysis of the transport properties which takes the classical fragmentation structure into account would also be useful^{25,28,33}. The behaviors of the bulk and boundary autocorrelation functions for a random thermal state in the thermodynamic limit also demands a more careful analysis in order to understand the nature of the freezing transition⁶⁵. Finally, it would be useful to study the effects of disorder^{61,70} and dissipation⁶⁶ in this model.

We expect that our results can be experimentally verified in cold-atom platforms^{71,72} where one-dimensional systems of spinless fermions with spatially periodic potentials and strong interactions can be realized. Recently, thermalization in some particular fragments of a model with HSF has been observed in a Rydberg atom system in one dimension⁷³. Another observation of HSF has been noted in a superconducting processor in a system demonstrating Stark many-body localization⁷⁴.

Acknowledgments

S.A. and D.S. thank Sanjay Moudgalya for helpful discussions. S.A. thanks MHRD, India for financial support through a PMRF. D.S. thanks SERB, India for funding through Project No. JBR/2020/000043.

Appendix A: Calculation of total number of fragments in the East model

We will compute here the total number of fragments N_{frag} in the East model using the transfer matrix method^{28–31,45}. We begin by observing that since our model comprises terms involving three consecutive sites, it is necessary to construct a 4×4 transfer matrix to compute the total number of fragments. We denote the matrix as $T_1(c_i, c_j)$, where c_i denotes the configurations 11, 10, 01 and 00 on two consecutive sites. In addition, as discussed earlier, a unique identification of the root state specifying each fragment requires us to move all occurrences of 10's to the left end of the system by successively changing 110's to 101's. This implies that any occurrences of 110 should be disallowed by the transfer matrix while counting the total number of fragments. After imposing this condition, the transfer matrix is found to be

$$T_1 = \begin{bmatrix} 1 & 0 & 0 & 0 \\ 0 & 0 & 1 & 1 \\ 1 & 1 & 0 & 0 \\ 0 & 0 & 1 & 1 \end{bmatrix}, \quad (\text{A1})$$

and the matrix $(T_1)^{L-2}$ leads to a construction of the root states from right to left for a system with L sites. The eigenvalues of T_1 are given by $\tau = (\sqrt{5} + 1)/2 \simeq 1.618$, $-1/\tau \simeq -0.618$, 1 and 0. The total number of fragments, therefore, grows exponentially with the system size as 1.618^L . We have confirmed this growth numerically as shown in Fig. (17).

Appendix B: Counting of frozen eigenstates in the East model

We will now count the total number of frozen eigenstates in the East model using a transfer matrix method^{28–31,45}. Following a similar procedure as in Appendix A, we construct another 4×4 transfer matrix, $T_2(c_i, c_j)$. However, the rule for constructing T_2 is different from the rule for T_1 . This is because for frozen eigenstates, both 110's and 101's should be disallowed by the transfer matrix. Upon imposing this rule, the transfer matrix is found to be

$$T_2 = \begin{bmatrix} 1 & 0 & 0 & 0 \\ 0 & 0 & 0 & 1 \\ 1 & 1 & 0 & 0 \\ 0 & 0 & 1 & 1 \end{bmatrix}. \quad (\text{B1})$$

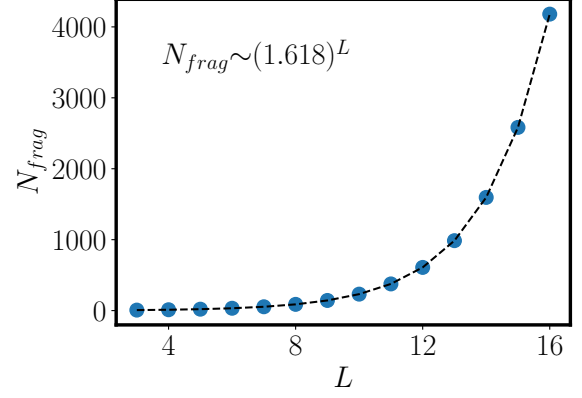


FIG. 17: Plot of the total number of fragments N_{frag} versus L , for a system with OBC. The numerical fitting shows that N_{frag} grows as 1.618^L .

The eigenvalues of Eq. (B1) are given by 1.466 , $-0.2328 \pm 0.7926i$ and 1. The number of frozen states, $N_{froz}(L)$ in our model, thus grows with system size as 1.466^L in the large- L limit. For the first few values of L , N_{froz} can also be computed by using the relation $N_{froz}(L) = \sum_{i,j} X_{i,j}$, where $X = T_2^{L-2}$; these values are shown in Table V. We also have $N_{froz}(L) = 1, 2, 4$ for $L = 0, 1$, and 2, respectively. We note that N_{froz} given in Table V for OBC follows the recursion relation $N_{froz}(L) = N_{froz}(L-1) + N_{froz}(L-3) + 1$ for $L \geq 3$.

It is also possible to calculate the number of frozen eigenstates for a system with PBC after incorporating the additional constraint that the four consecutive sites $(L-1, L, 1, 2)$ should not contain any occurrences of 110's and 101's. Imposing this rule, N_{froz} with PBC is given by

$$N_{froz} = X(1,1) + X(1,3) + X(1,4) + X(2,4) \\ + X(3,2) + X(3,4) + X(4,2) + X(4,3) \\ + X(4,4), \quad (\text{B2})$$

where $X = T_2^{L-2}$. The analytically obtained values of N_{froz} for PBC for the first few values of L are shown in Table V; these agree with the results obtained by numerical enumeration.

L	3	4	5	6	7	8	9	10
N_{froz}^{OBC}	6	9	14	21	31	46	68	100
N_{froz}^{PBC}	5	6	7	11	16	22	32	47

TABLE V: N_{froz} versus L with OBC and PBC as obtained analytically. These agree with our numerical results.

Appendix C: Recursive quantum scar states with zero entanglement at a non-central cut in the East model

We will now show that in some fragments, the recursive quantum scar states²⁵ can have zero entanglement at a cut which is not at the center of the system. In do so, we investigate a classical fragment originating from a root state 1010101011 for $L = 14$ and $N_f = L/2 + 1$. Our analysis shows that this fragment contains some exact quantum scar states. However, these states have zero entanglement, not at a central cut, but rather at a cut at $l = L/2 + 2$, as shown in Fig. 18. We have found four such zero-entangled states after following a similar method as discussed in the case of the largest fragment. We first note that there are two scar states with the entangled left-restricted part,

$$|\phi'_L\rangle = \frac{1}{\sqrt{3}}(|11100110\rangle - |11010101\rangle + |10111001\rangle), \quad (\text{C1})$$

while for the remaining two scar states, we have

$$|\phi'_L\rangle = \frac{1}{2}(|101111100\rangle - |110111010\rangle - |111100101\rangle + |111010110\rangle). \quad (\text{C2})$$

As in the previous case, $|\phi_R\rangle$ remains dynamically separated from $|\phi'_L\rangle$ by a $|00\rangle$. For the first two scar states, the Hamiltonian within the right-restricted part describes a tight-binding model with $L = 4$ and $N_f = 3$ with OBC. For the other two scar states, we get similar effective model with $L = 3$ and $N_f = 2$. In both cases, a single hole hops in the background of several particles, and the leftmost site, denoted l , of the right-restricted part remains frozen with $n_l = 1$. Hence, the single-particle energies in the first case are $E_p = -2 \cos(\pi p/4)$ with $p = 1, 2, 3$, and in the second case, $E_p = -2 \cos(\pi 3/p)$ with $p = 1, 2$; these are equal to $\pm 1.414, 0$ in the first case, and ± 1 in the second case. In Fig. 19 (a), we show the density profile of a scar state versus the site number within this fragment. As Fig. 19 (a) shows, the scar state has the form of a product state in the number basis ($|00\rangle$) on the 9-th and 10-th sites; this gives zero entanglement if the system is cut at $l = 9$ or 10, as illustrated in Fig. 19 (b). This state also has $S_l = 0$ for a cut at the 11-th cut since the leftmost site of the right-restricted part, $|\phi_R\rangle$, is frozen at $n_{i=11} = 1$. Next, we compare the scar states with a thermal state; where the density profile as a function of the site i and the entanglement S_l versus the location l of the cut of a thermal state are shown in Fig. 19 (c-d), respectively. In the latter case, we notice that the density profile continuously decreases with increasing site number. However, S_l first increases with l , reaches a maximum at $l = 9$, and then decreases with l , as we see in Fig. 19 (d); this cannot be explained in a simple way by the density profile illustrated in Fig. 19 (c).

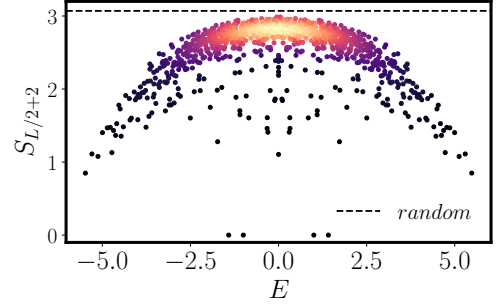


FIG. 18: Plot showing the entanglement spectrum versus E for the fragment generated from the root state 10101010101011 for $L = 14$ and $N_f = L/2 + 1$; the entanglement cut is made at $l = 9$ instead of at the center. We see that there are exactly four zero entanglement states in the middle of the spectrum. These states do not have zero entanglement if the cut is made at the center of the system.

Appendix D: Counting the total number of fragments in the PXXP+PYYP model

We will now discuss how to compute the total number of fragments $N_{frag}(L)$ in the PXXP+PYYP model using a transfer matrix method^{28-31,45}. Since this model allows transitions involving four consecutive sites, we need to construct a 8×8 transfer matrix, represented by $T_3(c_i, c_j)$ for our counting, c_i denotes the configurations 111, 110, 101, 011, 100, 010, 001 and 000 on three consecutive sites. Next, the root identification in this model requires successive removals of all occurrences of 1101's to uniquely define the fragments. Hence the transfer matrix should not allow the configuration 1101 to appear^{28-31,45}. We then find that the transfer matrix must have the form

$$T_3 = \begin{pmatrix} 1 & 1 & 0 & 0 & 0 & 0 & 0 & 0 \\ 0 & 0 & 0 & 0 & 1 & 0 & 0 & 0 \\ 0 & 0 & 0 & 1 & 0 & 1 & 0 & 0 \\ 1 & 1 & 0 & 0 & 0 & 0 & 0 & 0 \\ 0 & 0 & 0 & 0 & 0 & 0 & 1 & 1 \\ 0 & 0 & 1 & 0 & 1 & 0 & 0 & 0 \\ 0 & 0 & 0 & 1 & 0 & 1 & 0 & 0 \\ 0 & 0 & 0 & 0 & 0 & 0 & 1 & 1 \end{pmatrix}. \quad (\text{D1})$$

The eigenvalues of T_3 are given by 1.867 , -0.867 , $0.5 \pm 0.6067i$, and zero appearing four times. The total number of fragments, N_{frag} therefore grows as 1.867^L for large L . This agrees with our numerical results; see Fig. 20. We see that N_{frag} grows much faster in this model than in the East model. This can be understood from the fact the the infinite- V limit disallows some processes which the East model allows. Hence the degree of fragmentation in this model is larger in the infinite- V model.

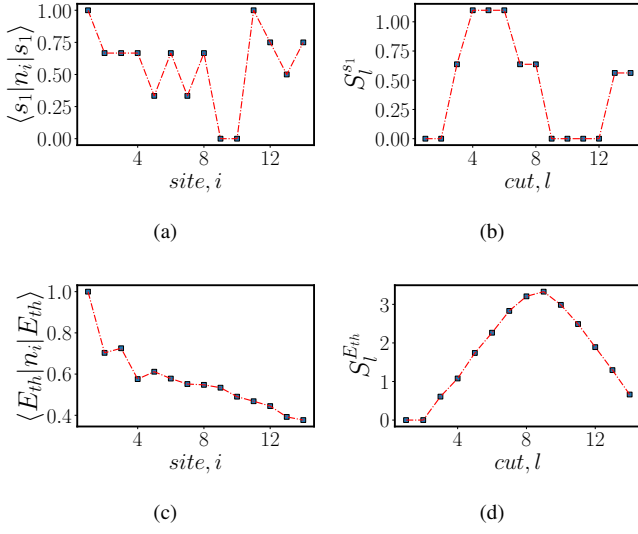


FIG. 19: (a) and (c): Variations of the expectation values of n_i versus the site number i in a scar state $|s_1\rangle$ and in a thermal state $|E_{th}\rangle$, both lying in fragment originating from the root state 10101010101011 for $L = 14$ and $N_f = L/2 + 1$. (b) and (d): Variation of the entanglement entropy S_l versus l for $|s_1\rangle$ and $|E_{th}\rangle$, respectively, for the same fragment as in plots (a) and (c). The density profile in plot (a) confirms that $|s_1\rangle$ has a product state form at sites 9 and 10. Further, the leftmost site of $|\psi_R\rangle$ is frozen at $n_j = 1$. These observations imply that the system will have zero entanglement for multiple locations of cuts, as we see in plot (b). On the other hand, a thermal state within this fragment shown in (c) demonstrates a distinct behavior since no part of the eigenstate has a product form. We observe that the minimum of the entanglement for $|s_1\rangle$ and the maximum of the entanglement for $|E_{th}\rangle$ appear when the cut is made at $l = 9$; these features are exactly opposite of each other.

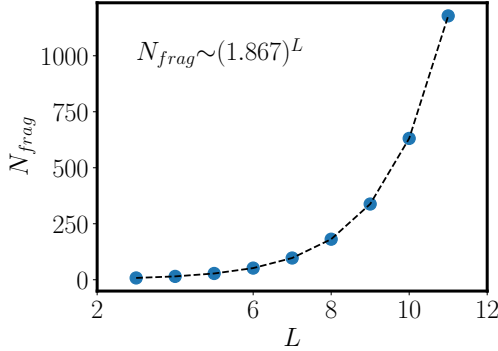


FIG. 20: Plot showing N_{frag} versus L for a system with OBC. The numerical fitting shows that N_{frag} grows as 1.867^L , which agrees with our analytically obtained result.

Appendix E: Counting of frozen eigenstates in the PXXP+PYYP model

We will now compute the number of frozen fragments¹¹ in this model using the transfer matrix method^{28–31,45}. We will

discuss this calculation for a system with OBC. The counting procedure again requires us to construct a 8×8 transfer matrix, similar to the construction shown in the calculation of the total number of fragments. However, the imposed rules to be imposed here are different from the previous one, namely, any occurrences of 1101 and 1011 must be disallowed as there can be transitions between these two; frozen states are dynamically inactive by definition. This rule leads to a transfer matrix $T_4(c_i, c_j)$ of the form

$$T_4 = \begin{pmatrix} 1 & 1 & 0 & 0 & 0 & 0 & 0 & 0 \\ 0 & 0 & 0 & 0 & 1 & 0 & 0 & 0 \\ 0 & 0 & 0 & 0 & 0 & 1 & 0 & 0 \\ 1 & 1 & 0 & 0 & 0 & 0 & 0 & 0 \\ 0 & 0 & 0 & 0 & 0 & 0 & 1 & 1 \\ 0 & 0 & 1 & 0 & 1 & 0 & 0 & 0 \\ 0 & 0 & 0 & 1 & 0 & 1 & 0 & 0 \\ 0 & 0 & 0 & 0 & 0 & 0 & 1 & 1 \end{pmatrix}, \quad (E1)$$

where c_i denotes the configurations 111, 110, 101, 011, 100, 010, 001 and 000 on three consecutive sites, as before. The eigenvalues of T_4 are given by 1.812, 1, $0.344 \pm 0.864i$, $-0.750 \pm 0.277i$, and zero appearing twice.. Hence, the total number of frozen states N_{froz} grows as 1.8124^L for large L . N_{froz} can be analytically computed by using the fact that $N_{froz} = \sum_{i,j=1}^8 Y_{ij}$, where $Y = T_4^{L-3}$, as shown in Table VI for a few values of L . We have verified that the analytical results agree with the results obtained by numerical enumeration. In addition, we have $N_{froz} = 1, 2, 4$ for $L = 0, 1$ and 2, respectively. We also note that N_{froz} follows a different recursion relation than the East model, which can be seen from Table VI, as

$$N_{froz}(L) = N_{froz}(L-1) + N_{froz}(L-2) + N_{froz}(L-4) + N_{froz}(L-5), \quad (E2)$$

for $L \geq 5$.

L	3	4	5	6	7	8	9	10	11
N_{froz}	8	14	25	45	82	149	270	489	886

TABLE VI: N_{froz} versus L as obtained analytically.

Appendix F: Computation of filling fraction for the ground state of the PXXP+PYYP model

We will now compute the filling fraction at which the ground state of the PXXP+PYYP model appears. We will do this by using the mapping to a non-interacting tight-binding model. Using the single-particle dispersion given in Eq. (31), the ground state energy for a specific fragment can be shown

to be

$$E_{GS} = -2 \sum_{n=1}^{N_B-1} \cos\left(\frac{\pi n}{N_A + N_B}\right). \quad (\text{F1})$$

Since we are interested in the ground state energy in the thermodynamic limit, i.e., $N_A, N_B \rightarrow \infty$, we can convert the summation in Eq. (F1) to an integration after defining a variable $x = n/(N_A + N_B)$. This yields

$$\begin{aligned} E_{GS} &= -2(N_A + N_B) \int_0^{\frac{N_B}{N_A+N_B}} dx \cos(\pi x) \\ &= -\frac{2}{\pi}(N_A + N_B) \sin\left(\frac{\pi N_B}{N_A + N_B}\right). \end{aligned} \quad (\text{F2})$$

We now note that the PXXP+PYYP model with a length $L = 2N_A + N_B$ and a filling fraction $\rho = (N_A + N_B)/L$ reduces to a tight-binding model with a length $L' = N_A + N_B$ and a filling fraction $\rho' = N_B/L'$. These relations imply that $\frac{1}{2} \leq \rho \leq 1$ in the original model, and $0 \leq \rho' \leq 1$ in the mapped model. Hence, rewriting N_A and N_B in terms of L and ρ , Eq. (F2) can be recast as

$$E_{GS} = \frac{2L\rho}{\pi} \sin\left(\frac{\pi}{\rho}\right). \quad (\text{F3})$$

We can now define a variable $y = \pi/\rho$, which lies between π and 2π ; we then have $E_{GS} = \frac{2L}{y} \sin y$. Extremizing E_{GS} with respect to y , we numerically find that the value of y at which E_{GS} has its minimum is $y_0 = 4.493$. Hence, the filling fraction at which the ground state lies in the PXXP+PYYP model is $\rho \simeq \pi/4.493 = 0.699$, and the ground state energy at this filling fraction is $E_{GS} \simeq 0.435 L$.

Appendix G: Robustness of quantum scars under various perturbations

We will now examine how robust the quantum many-body scars²⁵ are in the presence of various perturbations, specif-

ically, a nearest-neighbor density-density interaction with strength V , a random on-site potential taken from a uniformly distributed random numbers μ_j with zero mean, and a random hopping δJ_j on top of a uniform hopping $J = 1$ which is also taken from a uniform random distribution with zero mean. We note that all three perturbations keep the fragmentation structure of the East model unchanged. In Figs. 21 (a-c), we show the entanglement entropy versus the energy within the classical fragment generated from the root state 101010101011 for $L = 14$ and $N_f = L/2 + 1$ for a cut at the site $L/2 + 2$, in the presence of (a) $V = 0.1$, (b) $\mu_j = 0.1$, and (c) $\delta J_j = 0.1$, respectively. In Fig. 21 (a), with a small value of V , we see that the number of zero-entanglement states reduces to three from four for the unperturbed East model, as shown in Fig. 18. We show the density profile of one of these scar states in Fig. 21 (d). We find that this is very similar to what is seen in the East model in Fig. 19. For example, we see a state of the form $|001\rangle$ on the 9-th, 10-th and 11-th sites in both cases. In Fig. 21 (b), with a small random potential, we see that there are some scar states with small but non-zero entanglements. Specifically, we find that the entanglements are of order 10^{-2} , in contrast to the four scar states with exactly zero-entanglement (of order 10^{-15}) found in the unperturbed East model; see Fig. 18. The density profile of one of these scar states also looks a little different from the scar states of the East model. For instance, the state does not exactly have a $|001\rangle$ form at the 9-th, 10-th and 11-th sites as we see in Fig. 21 (e). In Fig. 21 (c), we observe that the scar states completely vanish when a small random hopping δJ_j is introduced; this is a very distinct behavior from the first two kinds of perturbations.

¹ C. Gross and I. Bloch, Quantum simulations with ultracold atoms in optical lattices, *Science* **357**, 995 (2017).
² A. Browaeys and T. Lahaye, Many-body physics with individually controlled Rydberg atoms, *Nature Physics* **16**, 132 (2020).
³ R. Blatt and C. F. Roos, Quantum simulations with trapped ions, *Nature Physics* **8**, 277 (2012).
⁴ G. Wendin, Quantum information processing with superconducting circuits: a review, *Reports on Progress in Physics* **80**, 106001 (2017).
⁵ F. Arute et. al., Quantum supremacy using a programmable superconducting processor, *Nature* **574**, 505 (2019).
⁶ M. Srednicki, Chaos and quantum thermalization, *Phys. Rev. E* **50**, 888 (1994).
⁷ J. M. Deutsch, Quantum statistical mechanics in a closed system, *Phys. Rev. A* **43**, 2046 (1991).

⁸ M. Rigol, V. Dunjko, and M. Olshanii, Thermalization and its mechanism for generic isolated quantum systems, *Nature (London)* **452**, 854 (2008).
⁹ A. Polkovnikov, K. Sengupta, A. Silva, and M. Vengalattore, Colloquium: Nonequilibrium dynamics of closed interacting quantum systems, *Rev. Mod. Phys.* **83**, 863 (2011).
¹⁰ D. A. Abanin, E. Altman, I. Bloch, and M. Serbyn, Colloquium: Many-body localization, thermalization, and entanglement, *Rev. Mod. Phys.* **91**, 021001(2019).
¹¹ S. Moudgalya, N. Regnault, and B. A. Bernevig, Entanglement of exact excited states of Affleck-Kennedy-Lieb-Tasaki models: Exact results, many-body scars, and violation of the strong eigenstate thermalization hypothesis, *Phys. Rev. B* **98**, 235156 (2018).
¹² M. Serbyn, D. A. Abanin, and Z. Papić, Quantum many-body scars and weak breaking of ergodicity, *Nature Phys.* **17**, 675

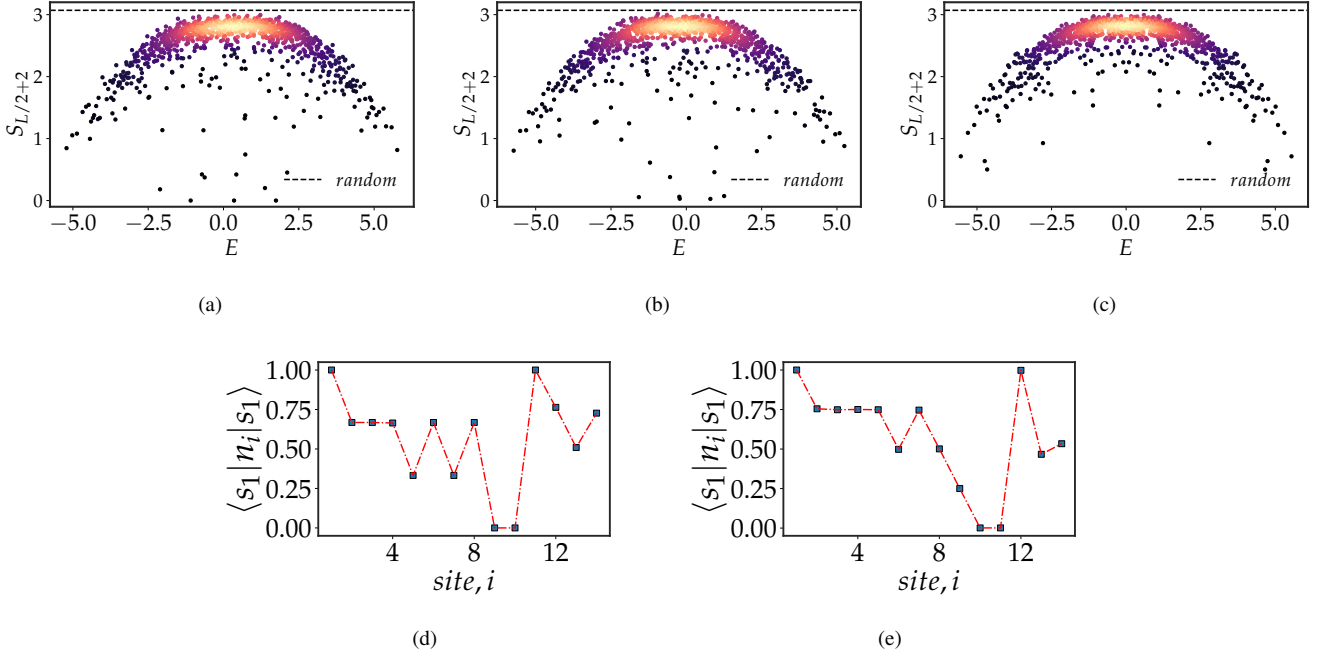


FIG. 21: (a-c) Plots showing the entanglement spectrum, $S_{L/2+2}$ versus E within the largest fragment originating from the root state 101010101011 for $L = 14$ and $N_f = L/2 + 1$, in the presence of three kinds of perturbations: (a) a nearest-neighbor density-density interaction $V = 0.1$, (b) a random on-site potential μ_j taken from a uniform distribution $[-0.1, 0.1]$ with zero mean, and (c) a random hopping of the form $1 + \delta J_j$, where δJ_j are random numbers taken from the uniform distribution $[-0.1, 0.1]$ with zero mean, respectively. Plot (a): we observe that having $V = 0.1$ reduces the number of zero-entanglement states to three from the four states found for the East model ($V = 0$) as shown in Fig. 18. However, the density profile for one of the scar states shown in plot (d) turns out to be similar to one of the scar states of the East model as shown in Fig. 19 (a). Plot (b): the entanglement of the scar states is not exactly zero when there is a random on-site potential. Namely, we find that the value of $S_{L/2+2}$ is of order 10^{-2} , unlike the states with exactly zero entanglement (numerically of order 10^{-15}) found for the East model. Further, these scar states do not have a perfect $|001\rangle$ form on the 9-th, 10-th and 11-th sites, as shown in plot (e). Plot (c): The scar states quickly vanish when a small random hopping is introduced.

- (2021).
- ¹³ M. Fagotti and F. H. L. Essler, Reduced density matrix after a quantum quench, *Phys. Rev. B* **87**, 245107 (2013).
 - ¹⁴ J. Preskill, Quantum Computing in the NISQ era and beyond, *Quantum* **2**, 79 (2018).
 - ¹⁵ T. Iadecola and M. Schechter, Quantum many-body scar states with emergent kinetic constraints and finite-entanglement revivals, *Phys. Rev. B* **101**, 024306 (2020).
 - ¹⁶ C. J. Turner, A. A. Michailidis, D. A. Abanin, M. Serbyn, and Z. Papić, Weak ergodicity breaking from quantum many-body scars, *Nature Phys.* **14**, 745 (2018).
 - ¹⁷ C.-J. Lin and O. I. Motrunich, Exact Quantum Many-Body Scar States in the Rydberg-Blockaded Atom Chain, Quantum many-body scars from magnon condensation, *Phys. Rev. Lett.* **122**, 173401 (2019).
 - ¹⁸ T. Iadecola, M. Schechter, and S. Xu, *Phys. Rev. B* **100**, 184312 (2019).
 - ¹⁹ S. Moudgalya, B. A. Bernevig, and N. Regnault, Quantum many-body scars and Hilbert space fragmentation: a review of exact results, *Rep. Prog. Phys.* **85**, 086501 (2022).
 - ²⁰ S. Moudgalya, B. A. Bernevig, and N. Regnault, Quantum many-body scars in a Landau level on a thin torus, *Phys. Rev. B* **102**, 195150 (2020).
 - ²¹ P. Sala, T. Rakovszky, R. Verresen, M. Knap, and F. Pollmann, Ergodicity Breaking Arising from Hilbert Space Fragmentation in Dipole-Conserving Hamiltonians, *Phys. Rev. X* **10**, 011047 (2020).
 - ²² V. Khemani, M. Hermele, and R. Nandkishore, Localization from Hilbert space shattering: From theory to physical realizations, *Phys. Rev. B* **101**, 174204 (2020).
 - ²³ S. Moudgalya and O. I. Motrunich, Hilbert Space Fragmentation and Commutant Algebras, *Phys. Rev. X* **12**, 011050 (2022).
 - ²⁴ L. Zadnik and M. Fagotti, The Folded Spin-1/2 XXZ Model: I. Diagonalisation, Jamming, and Ground State Properties, *SciPost Phys. Core* **4**, 010 (2021).
 - ²⁵ P. Brighi, M. Ljubotina, and M. Serbyn, Hilbert space fragmentation and slow dynamics in particle-conserving quantum East models, *SciPost Phys. Core* **15**, 093 (2023).
 - ²⁶ S. Moudgalya, A. Prem, R. Nandkishore, N. Regnault, and B. A. Bernevig, Thermalization and Its Absence within Krylov Subspaces of a Constrained Hamiltonian, *Memorial Volume for Shoucheng Zhang* (World Scientific, London, 2021), Chap. 7, pp. 147–209.
 - ²⁷ M. Borsi, L. Pristyák, and B. Pozsgay, Matrix Product Symmetries and Breakdown of Thermalization from Hard Rod Deformations, *Phys. Rev. Lett.* **131**, 037101 (2023).
 - ²⁸ M. Barma and D. Dhar, Slow Relaxation in a Model with Many Conservation Laws: Deposition and Evaporation of Trimers on a Line, *Phys. Rev. Lett.* **73**, 2135 (1994).
 - ²⁹ M. K. H. Menon and D. Dhar, The irreducible string and an infinity of additional constants of motion in a deposition-evaporation model on a line, *J. Phys. A* **28**, 6517 (1995).

- ³⁰ G. I. Menon, M. Barma, and D. Dhar, Conservation laws and integrability of a one-dimensional model of diffusing dimers, *J. Stat. Phys.* **86**, 1237 (1997).
- ³¹ S. Aditya, D. Dhar, and D. Sen, Subspace-restricted thermalization in a correlated-hopping model with strong Hilbert space fragmentation characterized by irreducible strings, *Phys. Rev. B* **110**, 045418 (2024).
- ³² A. Morningstar, V. Khemani, and D. A. Huse, Kinetically constrained freezing transition in a dipole-conserving system, *Phys. Rev. B* **101**, 214205 (2020).
- ³³ C. Wang and Z. C. Yang, Freezing transition in the particle-conserving East model, *Phys. Rev. B* **108**, 144308 (2023).
- ³⁴ H. Singh, B. A. Ware, R. Vasseur, and A. J. Friedman, Subdiffusion and Many-Body Quantum Chaos with Kinetic Constraints, *Phys. Rev. Lett.* **127**, 230602 (2021).
- ³⁵ J. Feldmeier, P. Sala, G. D. Tomasi, F. Pollmann, and M. Knap, Anomalous Diffusion in Dipole- and Higher-Moment-Conserving Systems, *Phys. Rev. Lett.* **125**, 245303 (2020).
- ³⁶ S. Aditya and D. Sen, Dynamical localization and slow thermalization in a class of disorder-free periodically driven one-dimensional interacting systems, *SciPost Phys. Core* **6**, 083 (2023).
- ³⁷ S. Ghosh, I. Paul, and K. Sengupta, Prethermal Fragmentation in a Periodically Driven Fermionic Chain, *Phys. Rev. Lett.* **130**, 120401 (2023).
- ³⁸ J. C. Howes, R. Senese, and A. Prakash, Universal Freezing Transitions of Dipole-Conserving Chains, [arXiv:2408.10321](https://arxiv.org/abs/2408.10321) (2024).
- ³⁹ T. Rakovszky, P. Sala, R. Verresen, M. Knap, and F. Pollmann, Statistical localization: From strong fragmentation to strong edge modes, *Phys. Rev. B* **101**, 125126 (2020).
- ⁴⁰ L. Caha and D. Nagaj, The pair-flip model: a very entangled translationally invariant spin chain, [arXiv:1805.07168](https://arxiv.org/abs/1805.07168).
- ⁴¹ S. Balasubramanian, S. Gopalakrishnan, A. Khudorozhkov, and E. Lake, Glassy Word Problems: Ultraslow Relaxation, Hilbert Space Jamming, and Computational Complexity, *Phys. Rev. X* **14**, 021034 (2024).
- ⁴² K. Adhikari and K. S. D. Beach, Deforming the Fredkin spin chain away from its frustration-free point, *Phys. Rev. B* **99**, 054436 (2019).
- ⁴³ K. Adhikari and K. S. D. Beach, Slow dynamics of the Fredkin spin chain, *Phys. Rev. B* **104**, 115149 (2021).
- ⁴⁴ O. Salberger and V. Korepin, Fredkin Spin Chain, [arXiv:1605.03842](https://arxiv.org/abs/1605.03842) (2016).
- ⁴⁵ R. L. Graham, D. E. Knuth, and O. Patashnik, Concrete Mathematics: A Foundation for Computer Science, 2nd ed. (Addison-Wesley, Amsterdam, 1994), Chap. 7.
- ⁴⁶ L. W. Shapiro, A Catalan triangle, *Discrete Mathematics* **14**, 83 (1976).
- ⁴⁷ V. Oganessian and D. A. Huse, Localization of interacting fermions at high temperature, *Phys. Rev. B* **75**, 155111 (2007).
- ⁴⁸ Y. Y. Atas, E. Bogomolny, O. Giraud, and G. Roux, Distribution of the Ratio of Consecutive Level Spacings in Random Matrix Ensembles, *Phys. Rev. Lett.* **110**, 084101 (2013).
- ⁴⁹ O. Bohigas, M.-J. Giannoni, and C. Schmit, Characterization of Chaotic Quantum Spectra and Universality of Level Fluctuation Laws, *Phys. Rev. Lett.* **52**, 1 (1984).
- ⁵⁰ C. M. Langlett and S. Xu, Hilbert space fragmentation and exact scars of generalized Fredkin spin chains, *Phys. Rev. B* **103**, L220304 (2021).
- ⁵¹ L. Causer, M. C. Bañuls, and J. P. Garrahan, Non-thermal eigenstates and slow relaxation in quantum Fredkin spin chains, *Phys. Rev. B* **110**, 134322 (2024).
- ⁵² F. Yang, H. Yarloo, H.-C. Zhang, K. Mølmer, and A. E. B. Nielsen, Probing Hilbert Space Fragmentation with Strongly Interacting Rydberg Atoms, [arXiv:2403.13790](https://arxiv.org/abs/2403.13790) (2024).
- ⁵³ X. Li, D. L. Deng, Y. L. Wu, and S. Das Sarma, Statistical bubble localization with random interactions, *Phys. Rev. B* **95**, 020201(R) (2017).
- ⁵⁴ L. Corcoran, M. D. Leeuw, and B. Pozsgay, Integrable models on Rydberg atom chains, [arXiv:2405.15848](https://arxiv.org/abs/2405.15848) (2024).
- ⁵⁵ N. Pancotti, G. Giudice, J. I. Cirac, J. P. Garrahan, and M. C. Bañuls, Quantum East Model: Localization, Nonthermal Eigenstates, and Slow Dynamics, *Phys. Rev. X* **10**, 021051 (2020).
- ⁵⁶ D. N. Page, Average entropy of a subsystem, *Phys. Rev. Lett.* **71**, 1291 (1993).
- ⁵⁷ M. V. Berry and M. Tabor, Level clustering in the regular spectrum, *Proc. R. Soc. Lond. Ser. A* **356**, 375 (1977).
- ⁵⁸ A. Vikram and V. Galitski, Dynamical quantum ergodicity from energy level statistics, *Phys. Rev. Research* **5**, 033126 (2023).
- ⁵⁹ E. P. Wigner, Characteristic Vectors of Bordered Matrices With Infinite Dimensions, *Ann. Math.* **62**, 548 (1955).
- ⁶⁰ M. Serbyn, A. A. Michailidis, D. A. Abanin, and Z. Papić, Power-Law Entanglement Spectrum in Many-Body Localized Phases, *Phys. Rev. Lett.* **117**, 160601 (2016).
- ⁶¹ L. Herviou, J. H. Bardarson, and N. Regnault, Many-body localization in a fragmented Hilbert space, *Phys. Rev. B* **103**, 134207 (2021).
- ⁶² Y. H. Kwan, P. H. Wilhelm, S. Biswas, and S. A. Parameswaran, Minimal Hubbard models of maximal Hilbert space fragmentation, [arXiv:2304.02669](https://arxiv.org/abs/2304.02669) (2023).
- ⁶³ S. Choi, C. J. Turner, H. Pichler, W. W. Ho, A. A. Michailidis, Z. Papić, M. Serbyn, M. D. Lukin, and D. A. Abanin, Emergent SU(2) Dynamics and Perfect Quantum Many-Body Scars, *Phys. Rev. Lett.* **122**, 220603 (2019).
- ⁶⁴ A. Udupa, S. Sur, S. Nandy, A. Sen, and D. Sen, Weak universality, quantum many-body scars, and anomalous infinite-temperature autocorrelations in a one-dimensional spin model with duality, *Phys. Rev. B* **108**, 214430 (2023).
- ⁶⁵ O. Hart, Exact Mazur bounds in the pair-flip model and beyond, *SciPost Phys. Core* **7**, 040 (2024).
- ⁶⁶ Y. Li, P. Sala, and F. Pollmann, Hilbert space fragmentation in open quantum systems, *Phys. Rev. Res.* **5**, 043239(2023).
- ⁶⁷ D. T. Stephen, O. Hart, and R. M. Nandkishore, Ergodicity Breaking Provably Robust to Arbitrary Perturbations, *Phys. Rev. Lett.* **132**, 040401 (2024).
- ⁶⁸ A. Yoshinaga, H. Hakoshima, T. Imoto, Y. Matsuzaki, and R. Hamazaki, Emergence of Hilbert Space Fragmentation in Ising Models with a Weak Transverse Field, *Phys. Rev. Lett.* **129**, 090602 (2022).
- ⁶⁹ O. Hart and R. Nandkishore, Hilbert space shattering and dynamical freezing in the quantum Ising model, *Phys. Rev. B* **106**, 214426 (2022).
- ⁷⁰ G. De Tomasi, D. Hetterich, P. Sala, and F. Pollmann, Dynamics of strongly interacting systems: From Fock-space fragmentation to many-body localization, *Phys. Rev. B* **100**, 214313 (2019).
- ⁷¹ I. Bloch, J. Dalibard, and W. Zwerger, Many-body physics with ultracold gases, *Rev. Mod. Phys.* **80**, 885 (2008).
- ⁷² T. Kohlert, S. Scherg, P. Sala, F. Pollmann, B. H. Madhusudhana, I. Bloch, and M. Aidelsburger, Experimental realization of fragmented models in tilted Fermi-Hubbard chains, [arXiv:2106.15586](https://arxiv.org/abs/2106.15586) (2021).
- ⁷³ L. Zhao, P. R. Datla, W. Tian, M. M. Aliyu, and H. Loh, Observation of quantum thermalization restricted to Hilbert space fragments, [arXiv:2403.09517](https://arxiv.org/abs/2403.09517) (2024).
- ⁷⁴ Y.-Y. Wang et al., Exploring Hilbert-Space Fragmentation on a Superconducting Processor, [arXiv:2403.09095](https://arxiv.org/abs/2403.09095) (2024).